Results in Engineering 30 (2026) 110727

Contents lists available at ScienceDirect

Results in Engineering

journal homepage: www.sciencedirect.com/journal/results-in-engineering

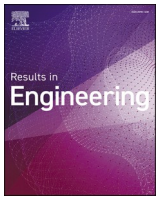

Research paper

Machine learning-assisted prediction of the hardness of additively manufactured and heat-treated Ti-6Al-4V alloy

Alireza Khanlari [a], Ali Reza Eivani [a,*], Morteza Zakeri [b], Jie Zhou [c], Hamid Reza Jafarian [a], Morteza Tayebi [a]

[a] School of Metallurgy and Materials Engineering, Iran University of Science and Technology, Tehran, Iran
[b] Department of Computer Engineering, Amirkabir University of Technology (Tehran Polytechnic), P. O. Box 159163-4311, Tehran, Iran
[c] Department of Biomechanical Engineering, Faculty of Mechanical Engineering, Delft University of Technology, Mekelweg 2, 2628 CD, Delft, the Netherlands

ARTICLE INFO

Keywords:
Selective laser melting (SLM)
Heat treatment
Ti-6Al-4V
Artificial intelligence algorithms
Machine learning

ABSTRACT

The optimization of post-processing heat treatment for selective laser melted Ti-6Al-4V remains challenging due to the strong nonlinear coupling between thermal history, microstructure, and hardness. Existing predictive models are typically limited by small datasets and narrow process coverage, particularly for post-heat-treatment hardness. In this study, a machine learning framework was developed to predict the Vickers hardness of heat-treated SLM Ti-6Al-4V using a curated multi-source dataset integrating experimental measurements (19 samples), literature-derived data (42), and 200 synthetically generated samples via Stratified Bootstrap combined with Gaussian Copula Noise. Fifteen regression models were systematically benchmarked using cross-validation. Among them, the Voting Regressor achieved the highest predictive accuracy ($R^2 \approx 0.92$, MAE $\approx$ 7.8 HV), demonstrating robust generalization across diverse heat-treatment conditions. Explainable artificial intelligence analysis revealed that microstructural characteristics and heat-treatment parameters are the dominant drivers of hardness, in agreement with phase-transformation mechanisms governing α' decomposition and $\alpha + \beta$ stabilization. The proposed framework provides a quantitative and interpretable tool for rational heat-treatment design of SLM Ti-6Al-4V, reducing reliance on empirical trial-and-error approaches and enabling data-driven process optimization.

1. Introduction

Additive manufacturing (AM), more commonly known as 3D printing, has advanced from creating samples and prototypes in a laboratory setting into a viable choice for producing functional and industrial parts [1]. Building parts in a layer-by-layer fashion eliminates many of the limitations of traditional manufacturing methods, most notably in shape complexity [2]. Unlike subtractive processes, such as machining, often resulting in significant waste of raw material, or formative processes such as casting and molding requiring molds, AM enables the direct production of finished or near-net-shape parts with high material efficiency without the need for tooling and within short lead time [3]. The ability to fabricate parts with complex geometries, including internal cavities or channels, and high customizability makes AM an attractive option for applications in the aerospace, medical, and energy industries [4,5]. Among various metal AM techniques, such as electron beam melting (EBM) [6], directed energy deposition (DED) [7,8], and binder jetting [9], selective laser melting (SLM) [10] holds a special place due to its high precision, localized high heat input, and ability to produce parts with high geometric complexity and near-bulk density [11]. Furthermore, with SLM, the mechanical and metallurgical properties of the part can be precisely controlled by changing process parameters, such as laser power, scan speed, hatch distance and layer thickness, which makes it particularly suitable for the products with high-performance requirements, such as those in aerospace and biomedical fields [12,13].

Ti-6Al-4V is the most widely used titanium alloy owing to its exceptional specific strength, corrosion resistance, thermal stability, and biocompatibility, enabling critical applications across aerospace, biomedical, and energy industries [14–16]. The widespread use of Ti-6Al-4V, combined with the manufacturing challenges associated with conventional processing of high-melting-point alloys, has made additive manufacturing, particularly SLM, a highly attractive route for producing complex components with improved efficiency and reduced machining

* Corresponding author.
E-mail address: aeivani@iust.ac.ir (A.R. Eivani).

https://doi.org/10.1016/j.rineng.2026.110727
Received 16 December 2025; Received in revised form 19 March 2026; Accepted 26 April 2026
Available online 26 April 2026

constraints [11,12]. Despite these advantages, SLM processing of Ti-6Al-4V often leads to the formation of metastable α′ martensite and significant residual stresses due to extremely high cooling rates and steep thermal gradients, resulting in microstructural heterogeneity and reduced ductility that can compromise structural reliability [1,11].

Post-SLM heat treatment is essential to minimize the microstructural heterogeneity, decompose the brittle α′ phase to form a balanced α + β phase microstructure, and eliminate residual stresses caused by the SLM process. As a result, post-SLM heat treatment improves the mechanical properties such as ductility and fracture toughness, and reduces anisotropy in the final part [1,17]. The selection of appropriate process parameter of heat treatment, including temperature (either below or above the β transus temperature), holding time, and cooling rate, plays a decisive role in achieving the desired properties. High temperature or long time may lead to grain growth and substantial loss of strength, while low temperature or insufficient time may not allow sufficient phase transformation to take place. The cooling method, including furnace cooling (FC), air cooling (AC), or quenching in water (QW), also has a direct effect on determining the final phase constituents and their distribution. The multi-parameter process makes the design of an optimal heat treatment scheme for the SLM Ti-6Al-4V alloy a technical challenge [1,12].

A lot of research efforts have been dedicated to understanding the effects of the process parameters of post-SLM heat treatment on the mechanical properties of Ti-6Al-4V. However, the vast majority of the studies are limited to fixed SLM process parameters or idealized SLM conditions without fully accounting for inevitable variations related to different AM setups and part geometries [18]. Moreover, while the metallurgical transformations and mechanical property changes due to post-SLM heat treatment have been qualitatively described, quantitative predictive models that integrate SLM process parameters with those of heat treatment are grossly underdeveloped. This gap limits the ability to tailor the mechanical properties of SLM Ti-6Al-4V products effectively without extensive experimental trials.

In this regard, the core problem lies that an optimum heat treatment scheme not only depends on the alloy composition itself but also differs between the parts produced under different manufacturing conditions (*e.g.*, variations in SLM process parameters or part geometry) [19]. This makes the design and experimental validation of heat treatment schemes for SLM Ti-6Al-4V parts a time-consuming, costly, and sometimes repetitive task. Therefore, in recent years, the development of new approaches to predicting and optimizing post-SLM heat treatment by using machine learning (ML) algorithms has been proposed as an effective means to address the issue that involves inherently complex thermal processes (both SLM and heat treatment) and nonlinear effects on the mechanical properties of the final part [17]. The rationale behind resorting to ML is obvious. Instead of relying solely on trial and error or physical simulations, ML algorithms have the ability to analyze existing data and provide patterns and predictions that are, in many cases, beyond the reach of traditional methods [20–22]. However, despite recent progress, some gaps remain. Most of existing models rely on limited data and sometimes experimental data only, which reduces their generalizability [4]. Although a number of studies [23–26] have already been performed in an attempt to predict the mechanical properties of SLM Ti-6Al-4V using ML, systematic integration of the process parameters of heat treatment, such as temperature, holding time, and cooling mode, alongside the SLM process variables, is lacking. Furthermore, many models were trained on limited datasets, which undermined their applicability across varied SLM process conditions. This calls for a comprehensive framework leveraging practical experimental data to accurately predict the as-heat-treated mechanical properties, thereby reducing the reliance on costly and time-intensive experimentation.

In the study conducted by Reddy *et al.* [27], artificial neural network (ANN) modeling of the flow stress of the annealed Ti-6Al-4V alloy with an equiaxed α + β microstructure under hot deformation conditions was performed. They used the back-propagation algorithm and the input parameters applied during hot deformation, including strain, strain rate, and temperature, and were able to predict the mean flow stress with an average error of 5.6 % across different two-phase regimes (*i.e.*, α + β to β phase). This model showed higher accuracy than classical equations, such as the sine hyperbolic relation, and was recommended for industrial applications. However, this model was limited to the prediction of flow stress during hot deformation and it did not consider prior material processing or its variations. In another study, Anand *et al.* [28] used three ML algorithms (*i.e.*, Random Forest (RF), Gradient Boosting, and XGBoost) and ANN to model the grinding process for the SLM Ti-6Al-4V alloy. They considered the input parameters such as cutting speed, feed rate, and depth of cut, and predicted the tangential force (*Fx*), normal force (*Fz*), temperature (*T*), and surface roughness (*Ra*) with reasonable accuracy. However, this study focused on the grinding process only and neglected the effects of SLM process parameters. Another study on ANN modeling of the heat-treated Ti-6Al-4V alloy to correlate the microstructural features with mechanical properties, carried out by Maurya *et al.* [29], attempted to predict the tensile properties of the alloy with microstructural variations and under different heat treatment conditions. The ANN used in this study was able to predict the ultimate tensile strength (UTS), yield strength (YS) and elongation (El %) with acceptable accuracy. Yet, the study did not incorporate preceding material processing parameters, including AM process parameters (wire arc AM and DED). In the research of Cao *et al.* [30], focusing on the optimization of SLM process parameters and microstructure tailoring, ML algorithms such as RF and XGBoost were used to predict the tensile properties of SLM Ti-6Al-4V samples. This approach was able to identify the effects of eight SLM parameters, such as scan speed and laser power, with high accuracy [30]. Still, the role of post-SLM heat treatment, although being a necessity for SLM Ti-6Al-4V, was not integrated into their predictive model. The overview presented above shows that while many studies have attempted to predict the as-fabricated mechanical properties of SLM Ti-6Al-4V, systematic modeling of the effect of post-SLM heat treatment on the mechanical properties using experimental data is underdeveloped. In particular, the effects of heat treatment process variables, such as temperature, holding time, and cooling mode, along with the process variables of SLM, has rarely been integrated into ML models.

To address these challenges, this study proposes an integrated experimental–data-driven framework for predicting the post-heat-treatment hardness of SLM-processed Ti-6Al-4V. Unlike previous studies [31–35] that primarily focused on tensile properties, as-built conditions, or limited datasets, the present work targets hardness evolution after heat treatment across diverse thermal conditions using a systematically curated and augmented dataset. The proposed framework combines controlled experimental measurements, literature-derived data integration, and statistically consistent synthetic data augmentation to construct a multi-source dataset representing a wide range of SLM processing parameters, heat-treatment conditions, and microstructural descriptors. Specifically, the dataset includes hardness measurements from experimentally produced samples, curated literature data, and additional synthetic samples generated using a variational autoencoder and correlation-preserving statistical augmentation. Based on this dataset, a systematic benchmarking of multiple regression algorithms—including linear models, tree-based methods, and neural networks—was performed to identify the most robust predictive strategy, with particular emphasis on ensemble learning approaches. Beyond prediction accuracy, explainable artificial intelligence techniques based on SHapley Additive exPlanations (SHAP) were employed to reveal the dominant metallurgical factors controlling hardness, enabling direct interpretation in terms of known phase-transformation mechanisms such as α′ martensite decomposition, α + β stabilization, and grain coarsening during heat treatment [23,36].

The novelty of the present work therefore lies not merely in incorporating heat-treatment parameters as additional model inputs, but in the structured integration of multi-source datasets, statistically controlled synthetic data generation that preserves feature correlations,

and interpretable ensemble learning for mechanistically consistent property prediction. This strategy enables both accurate hardness prediction and physically meaningful interpretation of process–structure–property relationships. Through this integrated workflow, the study establishes a robust and generalizable predictive model for post-heat-treatment hardness of SLM Ti-6Al-4V and provides actionable guidance for rational heat-treatment design. By reducing reliance on empirical trial-and-error experimentation, the proposed framework offers a practical pathway toward accelerated, data-driven optimization of additive manufacturing processes.

2. Material and methods

2.1. Starting material

A grade 5 Ti-6Al-4V alloy powder supplied by AP&C, Canada, and produced by using gas atomization was used in the current study. Its chemical composition is given in Table 1. The morphology was examined using a scanning electron microscope (SEM) and the particle size distribution of the powder was determined from SEM images. The results are presented in Fig. 1. As can be seen, the particles had an almost spherical shape – a characteristic that is considered desirable for SLM. The sizes of powder particles fell into the range of 13.4 to 44.3 μm with the average diameter being 29.1 μm and the standard deviation being 7.1 μm.

2.2. Sample preparation

Samples were produced using an EP-M250 3D metal printer manufactured by Eplus, China. The SLM process was carried out in a closed chamber and under the argon shielding gas to prevent oxidation and surface contamination of the powder. The oxygen concentration in the printing chamber was set at lower than 500 ppm to minimize unwanted reactions. The laser power applied was 180 W, scan speed 1000 mm/s, hatch distance 0.12 mm, and layer thickness 30 μm.

2.3. Heat treatment

Post-SLM heat treatment was performed in a laboratory electric furnace (model TF5/25–1500 supplied by AZAR Furnaces, Iran) with precise temperature control. The furnace chamber was filled with high-purity argon gas at a flow rate of 0.5 L/min to prevent the samples from oxidation at the surface. Heating rate was chosen to be 5 °C/min at all stages. The heat treatment of Ti-6Al-4V samples was performed in two groups. (i) Isothermal heat treatments were performed by heating the samples to one of four different temperatures (1050, 950, 850, or 750 °C), holding at that temperature for 2 h, followed by three different modes of cooling: FC, AC, and QW, and a total of 12 samples were included in this group. (ii) Two-stage (duplex) heat treatments: samples (No. 13, 14 and 15) were heated at 950 °C for 2 h, t cooling was carried out under three different conditions, including FC, AC, and QW, and then aging occurred at 650 °C for 2, 4, and 8 h, followed by air cooling. The samples (No. 16, 17 and 18) were first heated at 1050 °C for 2 h, followed by cooling in the furnace. Then, aging was performed at 950 °C for 2 h, followed by cooling in the three different modes. In total, the duplex heat treatments included 6 samples. Table 2 provides a complete list of the process parameters of the heat treatments applied to the 18 samples in addition to the as-SLM-fabricated sample.

Metallographic samples were prepared by grinding with abrasive sandpaper having 600–2000 grits and then polishing using an alumina solution, followed by final polishing with a diamond paste to achieve a mirror surface without scratches. The samples were etched using Kroll's reagent (containing 2 mL hydrofluoric acid, 6 mL nitric acid, and 92 mL distilled water) for 10 to 15 s. Finally, microscopic imaging was performed using an HUVITZ optical microscope (model HR3-TRF-P, South Korea).

2.4. Hardness tests

To investigate the effects of the heat treatment variables on the microstructure and mechanical properties of the Ti-6Al-4V alloy samples, Vickers hardness tests were performed using a Shab Sari microhardness tester (Model M5, Iran) under a loading force of 1000 g for 10 s. For each sample, the hardness test was repeated at least three times. The average of the measurements is reported as the final value along with the standard error of the average value.

2.5. Machine learning (ML)

2.5.1. Data collection and preprocessing

Following initial preprocessing and the removal of incomplete records, the dataset was built from two main sources: 42 samples extracted from published literature covering various SLM process parameters, and 19 in-house experimental samples. For the experimental portion, Vickers hardness was measured at three separate indents per condition, with enough spacing left between indents to prevent work-hardening interference.

To strictly prevent data leakage, all 61 real samples were merged into a single pool before applying a stratified 80/20 train-test split. As detailed in Fig. 2a, this split set aside 11 real samples exclusively for testing, leaving 50 for training. Importantly, the synthetic data generation was applied only to this training subset. Keeping the test set comprised entirely of real, unseen samples ensured that the final model evaluations remained completely unbiased.

Training a model with 30 features on just 50 real samples creates a severely underdetermined system, which typically leads to overfitting. To resolve this data scarcity, 200 synthetic samples were generated using a Stratified Bootstrap approach combined with Gaussian Copula Noise. This specific technique helps preserve the complex correlations between features while injecting realistic variance. The statistical validity of these synthetic samples was checked using the Kolmogorov-Smirnov (KS) test (Fig. 2b). Since the KS statistics for the key parameters stayed well below the accepted threshold, the synthesized distributions were considered statistically reliable. experimental setup: (i) the material had to be Ti-6Al-4V produced via SLM; (ii) heat treatment temperatures and holding times had to be clearly reported; (iii) the cooling mode had to be specified; and (iv) final hardness values (HV) had to be explicitly stated or extractable from figures. The final combined dataset contains 30 independent features (Table 3), spanning SLM process parameters, heat treatment conditions, microstructural features (*e.g.*, grain size), and final hardness. During the in-house experiments, the SLM parameters were deliberately fixed to isolate and study the effects of heat treatment. However, integrating the literature data introduced necessary variability in parameters like laser power and scan speed. This multi-source integration allowed the machine learning models to learn from a much broader operational window rather than being limited to the experimental campaign alone. Although data augmentation expanded the training pool, there was a risk of amplifying the noise or reporting biases commonly found in multi-source literature data. To mitigate this, the physical validation of the synthetic data was

Table 1
Chemical composition of the Ti-6Al-4V alloy powder.

Element	Y	H	N	C	O	Fe	V	Al	Ti
wt. %	0.001	0.002	0.017	0.014	0.064	0.22	4.0	6.3	Bal.

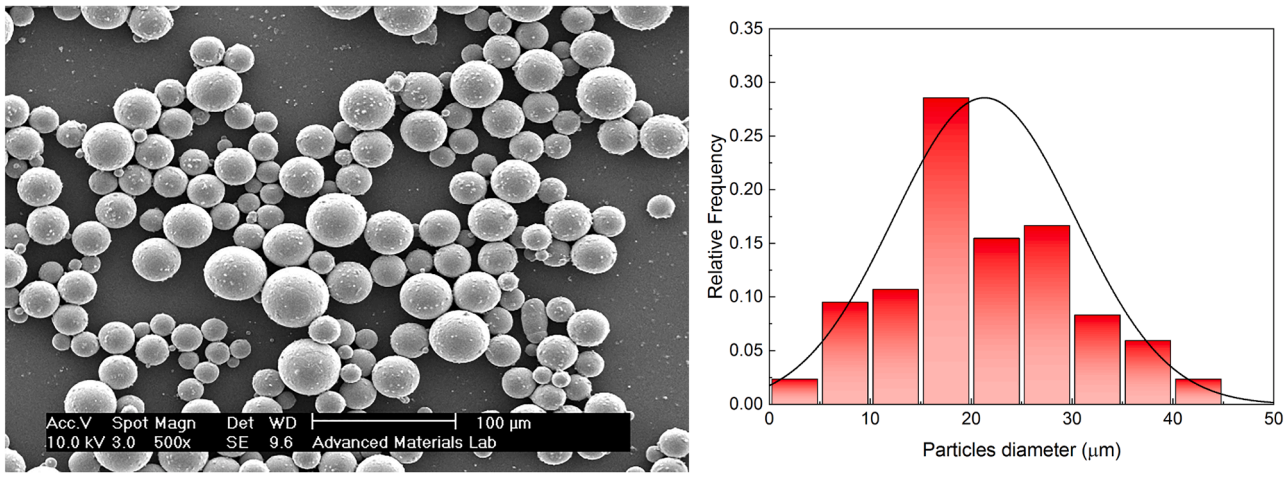

Fig. 1. SEM micrograph of the Ti-6Al-4V alloy powder and the histogram of its particle size distribution.

Table 2
Temperature, time, and cooling conditions of the heat treatments applied to the 18 samples.

Cycle	Sample	Heat treatment type	First stage temperature (°C)	First stage cooling	First cooling stage time (h)	Second stage temperature (°C)	Second cooling stage time (h)	Second stage cooling
HT-A	1	Isothermal	750	FC	2	-	-	-
	2	Isothermal	750	AC	2	-	-	-
	3	Isothermal	750	QW	2	-	-	-
HT-B	4	Isothermal	850	FC	2	-	-	-
	5	Isothermal	850	AC	2	-	-	-
	6	Isothermal	850	QW	2	-	-	-
HT-C	7	Isothermal	950	FC	2	-	-	-
	8	Isothermal	950	AC	2	-	-	-
	9	Isothermal	950	QW	2	-	-	-
HT-D	10	Isothermal	1050	FC	2	-	-	-
	11	Isothermal	1050	AC	2	-	-	-
	12	Isothermal	1050	QW	2	-	-	-
HT-E	13	Duplex	950	FC	2	650	2	AC
	14	Duplex	950	AC	2	650	4	AC
	15	Duplex	950	QW	2	650	8	AC
HT-F	16	Duplex	1050	FC	2	950	2	FC
	17	Duplex	1050	FC	2	950	2	AC
	18	Duplex	1050	FC	2	950	2	QW

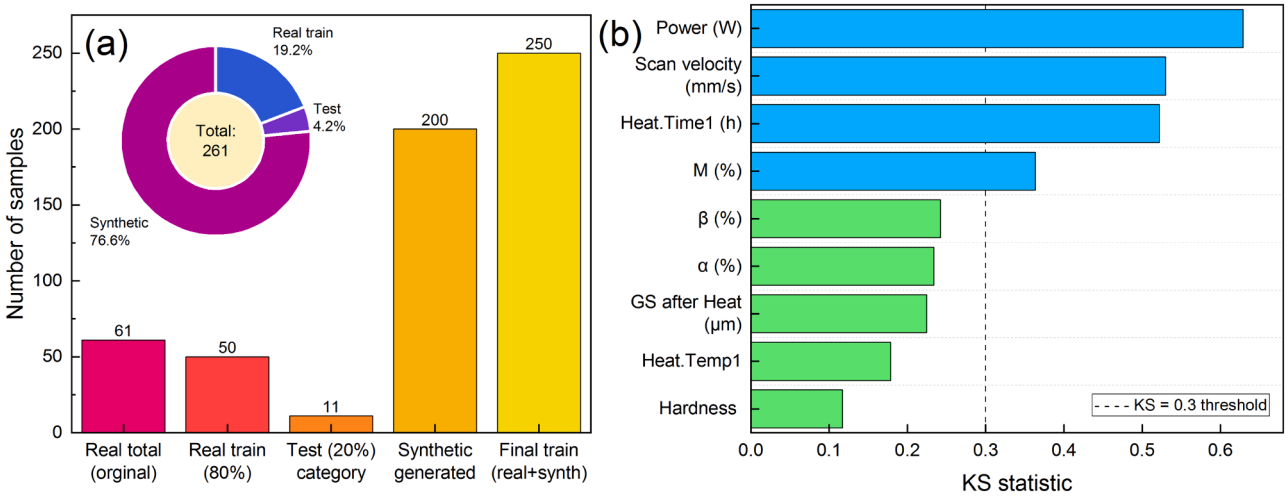

Fig. 2. (a) Dataset split and number of samples for each category and (b) KS test results.

deliberately anchored to the 19 high-fidelity experimental samples, which served as a reliable ground truth. This validation is presented in Fig. 3. The Principal Component Analysis (PCA) in Fig. 3a plots the 200 synthetic samples directly against these 19 experimental points (n = 19), demonstrating that the generated data tightly follows the actual physical clusters without scattering randomly. Likewise, the hardness

Table 3
Selected features for ML input.

No.	Features	No.	Features
1	Ti	16	Hatch distance
2	Fe	17	Layer thickness (μm)
3	V	18	Heat.Temp1 (°C)
4	Al	19	Heat.Time1 (h)
5	H	20	Heat.Temp2 (°C)
6	N	21	Heat.Time2 (h)
7	O	22	Cooling1_Air Cooling
8	C	23	Cooling1_As-Built
9	α %	24	Cooling1_FurnaceCooling
10	β %	25	Cooling1_Quench Water
11	M %	26	Cooling2_Air Cooling
12	Grain size before Heat (μm)	27	Cooling_As-Built1
13	Grain size after Heat (μm)	28	Cooling2_As-Built
14	Power (W)	29	Cooling2_FurnaceCooling
15	Scan velocity (mm/s)	30	Cooling2_Quench Water

density distribution (Fig. 3b) confirms that the synthetic data accurately mimics the real experimental hardness profile.

2.5.2. *Theoretical foundation of the machine learning framework*

To ensure methodological rigor, the adopted regression models are briefly introduced from a theoretical perspective.

- Linear Regression (LR)

Linear regression assumes a linear relationship between input features x and the target hardness (y) [37]:

$$y = ax + b \tag{1}$$

The coefficient b represents the slope of the linear relationship, while a denotes the intercept, corresponding to the value of y when $x = 0$. In this formulation, x may denote either a single input variable or multiple features that jointly influence the response variable y. The parameters of the model are determined by minimizing the mean squared error (MSE) [37].

$$\frac{1}{N}\sum_{i=1}^{N}\left(y_i - y_p\right)^2 \tag{2}$$

This metric is calculated by taking the squared difference between the actual value of the target variable (y_i) and the model prediction (y_p) for each observation, summing these squared deviations across all data points, and then dividing by the total number of samples (N). Such a linear model provides a baseline framework for assessing the relationship between processing parameters and hardness.

- Support Vector Regression (SVR)

SVR seeks a function $f(x)$ that deviates from the true target by at most ε while maintaining maximal flatness [38]:

$$\underset{\omega \in R^n b \in R^1}{min} \frac{1}{2}\| w \|^2 + C\sum_{s=1}^{L}\left(l(\xi_s) + l(\xi_s')\right) \tag{3}$$

subject to:

$$y_s - \omega^T\varphi(x_s) - b \le \xi_s + \varepsilon \tag{4}$$

$$\omega^T\varphi(x_s) + b - y_s \le \xi_s' + \varepsilon \tag{5}$$

$$\forall_s \in \{1, \ldots, L\} \tag{6}$$

where $\varphi(x)$ maps inputs into a high-dimensional feature space via a kernel function. SVR is particularly suitable for capturing nonlinear process–property relationships.

- Tree-Based and Ensemble Models

Decision trees partition the feature space recursively by minimizing impurity metrics such as MSE. For a node split [39]:

$$\mathrm{MSE} = \frac{1}{N}\sum_{i=1}^{N}(y_i - y')^2 \tag{7}$$

Random Forest aggregates multiple decorrelated trees via bootstrap sampling and averaging [40]:

$$\hat{y} = \frac{1}{T}\sum_{t=1}^{T} f_t(x) \tag{8}$$

Gradient Boosting constructs additive models sequentially [41]:

$$F_m(x) = F_{m-1}(x) + \gamma_m\, h_m(x) \tag{9}$$

where each weak learner (h_m) fits the negative gradient of the loss function. This sequential error-correction mechanism enables effective modeling of highly nonlinear interactions between SLM parameters and heat-treatment variables.

- SHAP interpretability

SHAP explains model predictions using additive feature attribution [42]:

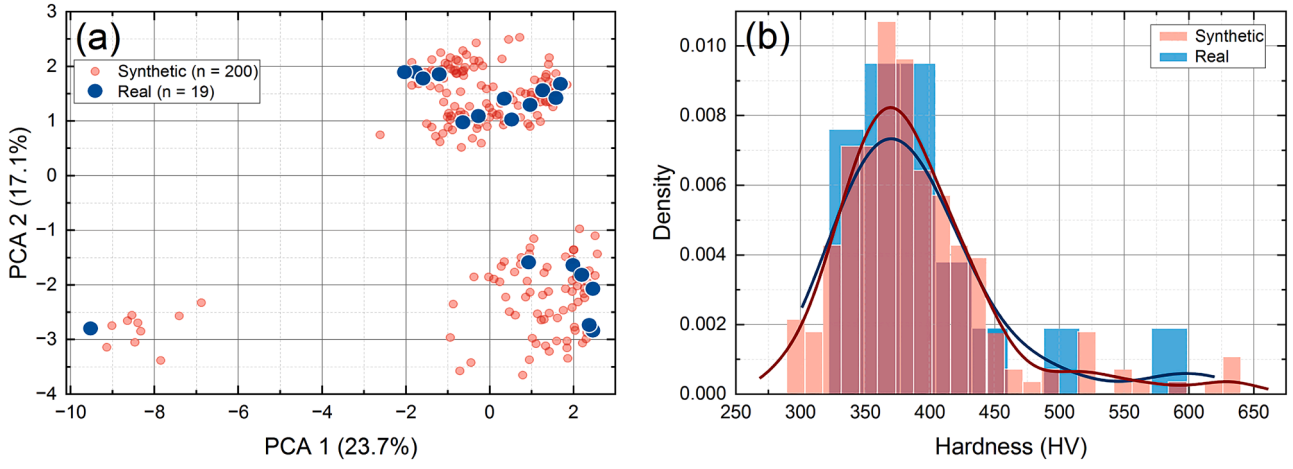

Fig. 3. (a) PCA design space coverage and (b) hardness distributions for real and synthetic data.

$$g(x') = \emptyset_0 + \sum_{i=1}^{M} \emptyset_i z'_i \quad (10)$$

where $\emptyset_i$ represents the Shapley value of feature (i), quantifying its marginal contribution averaged over all feature coalitions. This provides a theoretically grounded interpretability framework based on cooperative game theory.

2.5.3. Computational workflow

The overall computational framework is illustrated schematically in Fig. 4 and consists of the following stages:

1. Data acquisition: Experimental hardness measurements (19 samples) were generated under controlled heat-treatment conditions. Literature-derived data were curated based on consistency criteria.
2. Data preprocessing: Missing values were handled, categorical variables encoded, and features normalized.
3. Synthetic data augmentation: A Stratified Bootstrap combined with Gaussian Copula Noise a method that preserves the inter-feature correlation structure while introducing realistic variance.
4. Feature engineering: Input features included SLM process parameters, alloy composition, and multi-stage heat-treatment variables.
5. Model benchmarking: fifteen regression algorithms were trained using k-fold cross-validation.
6. Performance evaluation: Models were assessed using R^2, MAE, and RMSE on unseen test data
7. Interpretability analysis: SHAP was employed to identify dominant drivers of hardness.

Fig. 5 illustrates the SHAP plot of the VoR. It revealed that the most influential factors in the model's predictions are the parameters related to the heat-treatment process and microstructure. In particular, the feature M % had by far the greatest importance, and the value obtained from SHAP analysis indicated that a higher M % strongly increased the model's output. Following this feature, the features of Heat.Temp2 (°C) and grain size after heat treatment (μm) also played a significant role, with higher values likewise contributing positively to the model predictions. These finding highlights that the microstructure and Heating process, especially its martensite, temperature and grain size, acts as the primary driver of the model's outcomes. Other features, such as Heat. Time1 (h) and Cooling1_Furnace Cooling also exhibited notable importance, although their effects were considerably weaker in comparison to the microstructure parameters. In contrast, many other features, such as cooling-related parameters (*i.e.*, Cooling1_Air Cooling and Cooling1_As-Built) as well as the material's chemical composition (*i.e.*, the percentages of elements such as Al, V, Ti, and C), had negligible influences on the model's output. Their SHAP values were close to zero, indicating that the variations of these features had virtually no impacts on the predictions.

In conclusion, the analysis of the SHAP plot provides the insight that, for this specific dataset, the VoR model bases its decisions primarily on the microstructure and heat-treatment parameters. This deepens the understanding of the model's behavior and suggests that, for improving results or optimizing the physical process, focusing on temperature and microstructure is far more effective than adjusting other parameters.

It is important to clarify that the contribution of this study does not simply consist of incorporating heat-treatment parameters as additional inputs to conventional regression models. Prior ML studies have indeed included processing variables for property prediction. The fundamental advancement presented here lies in the structured integration of heterogeneous data sources, statistically consistent Stratified Bootstrap combined with Gaussian Copula Noise, and interpretable ensemble learning specifically tailored to post-heat-treatment hardness modeling. Unlike earlier works that relied on single-source experimental datasets

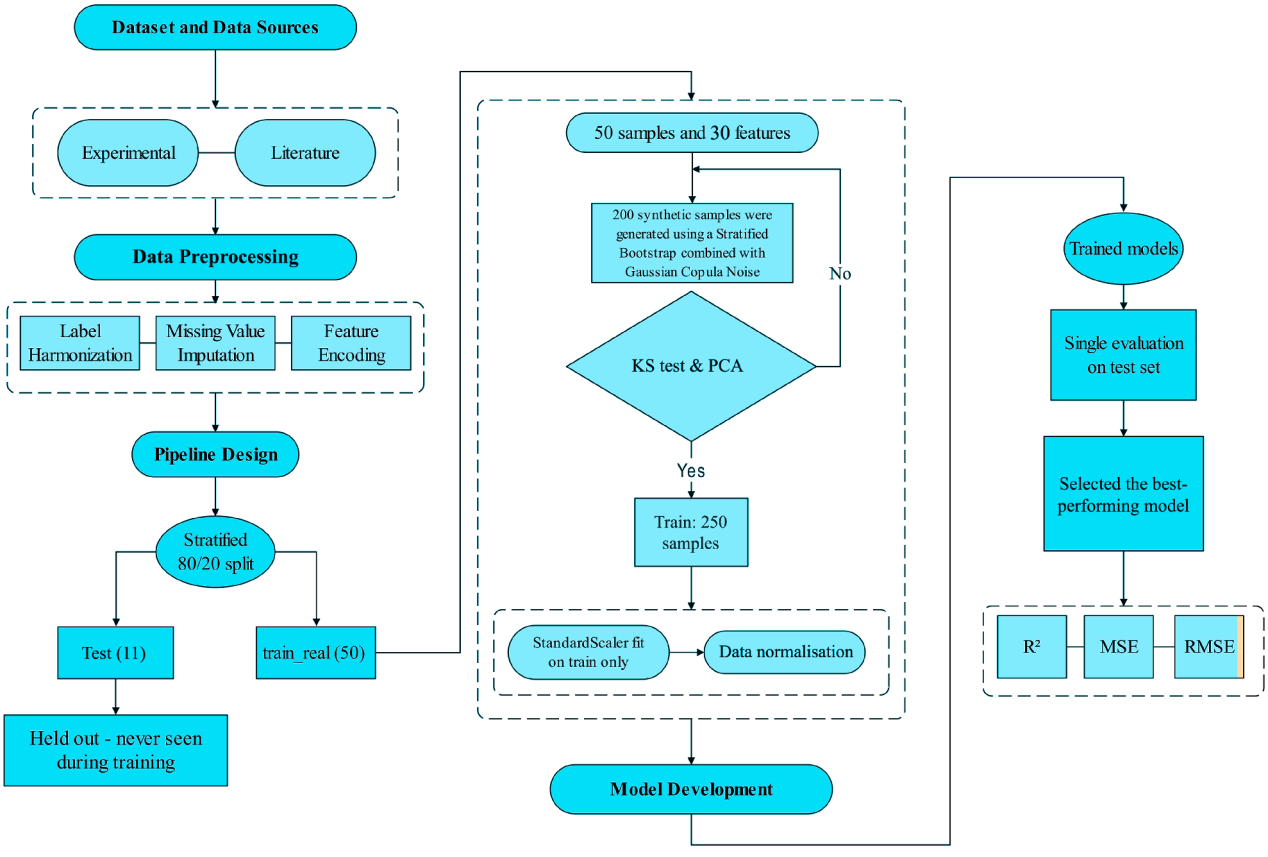

Fig. 4. The algorithmic framework of this study.

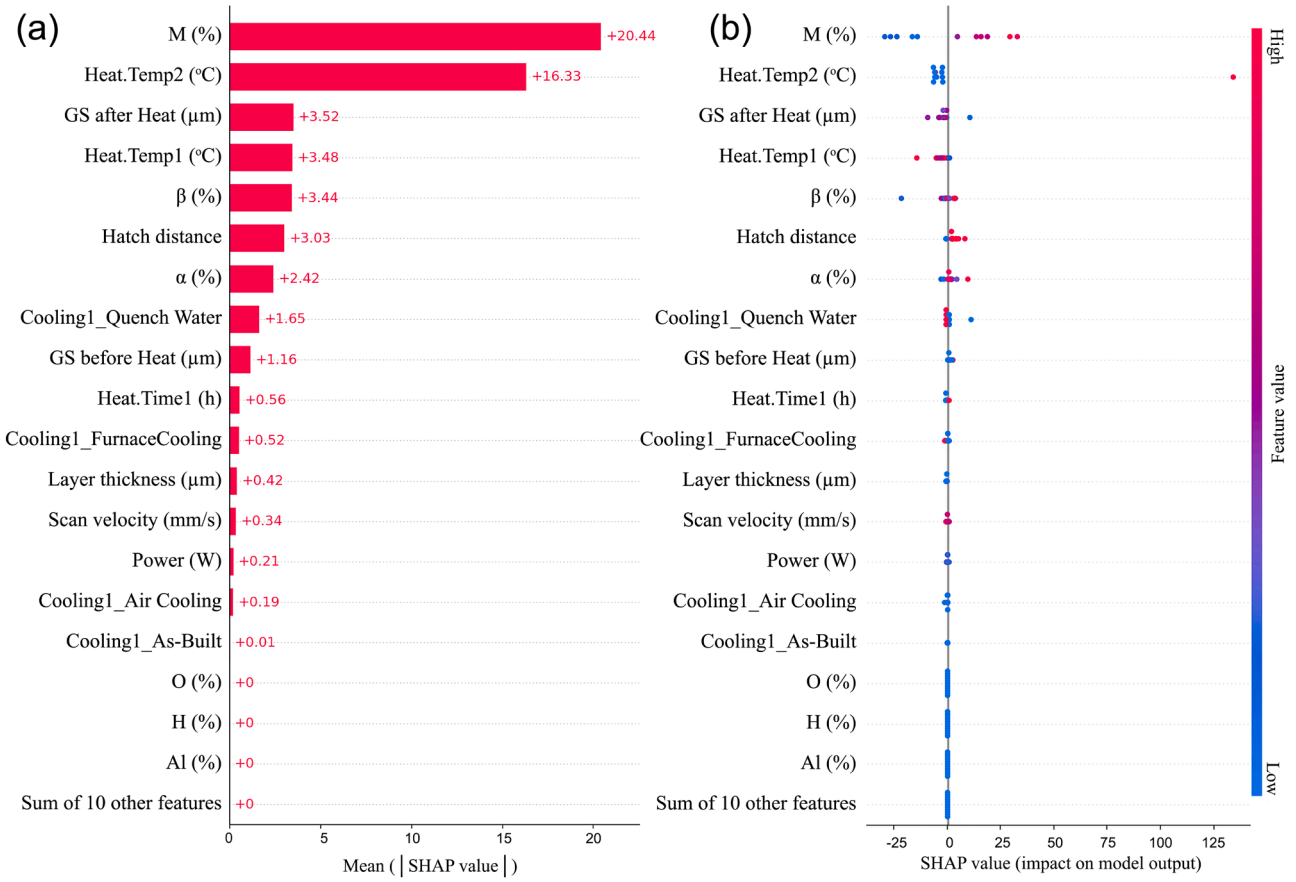

Fig. 5. The SHAP plot of the VoR: (a) mean SHAP value and (b) SHAP value impact on model output.

with limited statistical coverage, the present framework establishes a unified multi-source dataset architecture, enabling broader representation of thermal conditions. Furthermore, the incorporation of SHAP-based interpretability bridges data-driven predictions with established phase-transformation mechanisms, providing mechanistic insight rather than purely black-box regression (Figs. 5 and 6). This combination of data architecture, ensemble benchmarking, and physically interpretable modeling constitutes the primary methodological contribution of the study.

2.5.4. *Feature ablation and stability analysis*

To strengthen the interpretability claims beyond SHAP-based attribution, additional ablation and stability analyses were conducted.

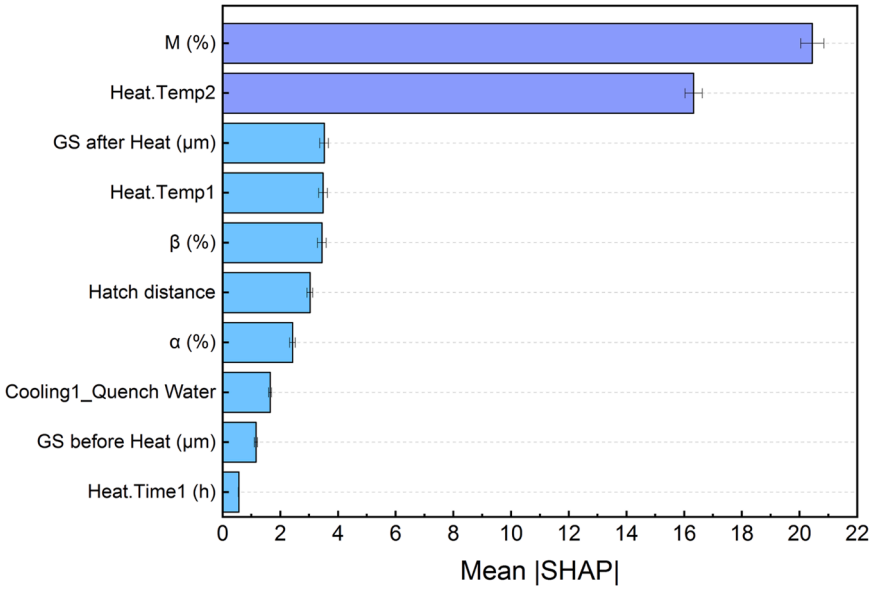

Fig. 6. Mean SHAP value for important features.

- **Ablation analysis**

The top-ranked features identified by SHAP (second-stage heat-treatment, cooling type, SLM parameters, all heat treatment features, and synthetic) were systematically removed from the input set, and the VoR model was retrained under identical cross-validation conditions. Removal of the second-stage temperature resulted in a significant reduction in predictive performance (R^2 decreased from 0.896 to 0.202), while removing cooling type and SLM parameters R^2 keep constant. These results quantitatively confirm that the identified variables are not merely correlated but are critical contributors to predictive accuracy. A feature-group ablation study quantified each component's contribution. Each condition removes one group, retrains from scratch using the identical pipeline, and reports test R^2 in Fig. 7.

- **Stability of feature importance**

To assess robustness, SHAP importance rankings were evaluated across five cross-validation folds and multiple random splits. The top two features consistently ranked first and second, with low variance in mean absolute SHAP values. This stability indicates that the interpretability results are not artifacts of a particular data partition. Together, these analyses support the reliability of the identified dominant drivers and strengthen the interpretability of the proposed framework. SHAP-based analysis suggests consistency with established metallurgical transformations, while acknowledging that statistical attribution does not replace direct microstructural characterization.

The inter-feature correlations for this curated dataset are presented in Fig. 8. All continuous features were standardized, categorical features, such as cooling mode, were one-hot encoded, and outliers were removed after statistical analysis. Correlation analysis was conducted to identify potential multicollinearity and to examine the relationships between the selected features and hardness.

2.5.5. Model development and evaluation

The purpose of using ML algorithms was to model the relationships of the SLM and heat treatment process parameters with the microstructural features and mechanical properties of the as-heat-treated Ti-6Al-4V alloy. Model performance metrics were calculated using the independent real experimental test data. To ensure the repeatability of the results, random_state = 42 was set in all randomization steps, including data partitioning and modeling algorithms. To evaluate the performance of the models, in addition to advanced ML algorithms, a baseline model was also used to clarify the role of real learning in improving the prediction. This baseline model was a Dummy Regressor, which always outputs the average hardness value of the training data.

Model screening involved fifteen distinct models: Multi-Layer Perceptron (MLP), Support Vector Regressor (SVR), Decision Tree (DT), Random Forest (RF), AdaBoost (with DT and XGBoost estimators), Voting Regressor (VOR), Gradient Boosting Regressor (GBR), Hist-Gradient Boosting Regressor (HGBR), K-Nearest Neighbors (KNN), Stacking Regressor (StR), linear Bayesian Ridge (LBR), Stochastic Gradient Descent Regressor (SGDR), DADA (with AdaBoost and DT) and XGBoost, Dummy Regressor. Hyperparameters (Table 4) for four of the models were systematically tuned using grid search with cross-validation (GridSearchCV).

After comparing the fifteen different algorithms, including linear models, tree-based methods, neural networks, and boosting techniques, the results indicated that gradient-based models (VoR and HGBR) achieved the best performance in predicting the hardness of the Ti-6Al-4V alloy. These models not only exhibited the highest coefficient of determination (R^2) values but also yielded lower mean absolute error (MAE) and mean square error (MSE), as compared to the other algorithms. Furthermore, the consistency of the results across multiple cross-validation runs demonstrated their strong generalization capability to unseen data. In contrast, simpler models such as DT, despite their interpretability, suffered from overfitting and consequently showed weaker performance on the test set. Therefore, VoR was selected as the final model.

For hyperparameter optimization, a systematic grid search strategy combined with five-fold cross-validation was employed. In this framework, the dataset was partitioned into five subsets, of which, in each iteration, four subsets were used for model training and the remaining one for validation. This systematic evaluation across different data partitions ensured robust assessment of the candidate hyperparameter configurations and mitigated the risk of arbitrary parameter selection. As a result, the generalization capability of the model to unseen data was improved, while the likelihood of overfitting was substantially reduced.

The dataset was split into training and testing subsets at an 80/20 ratio and five-fold cross- validation was employed to improve reliability. Model performance was evaluated using R^2, MAE, and MSE.

One of the major challenges in modeling experimental data is the risk of overfitting, a situation in which the model memorizes specific patterns of the training set rather than capturing the underlying general relationships. In this study, several strategies were employed to mitigate this risk:

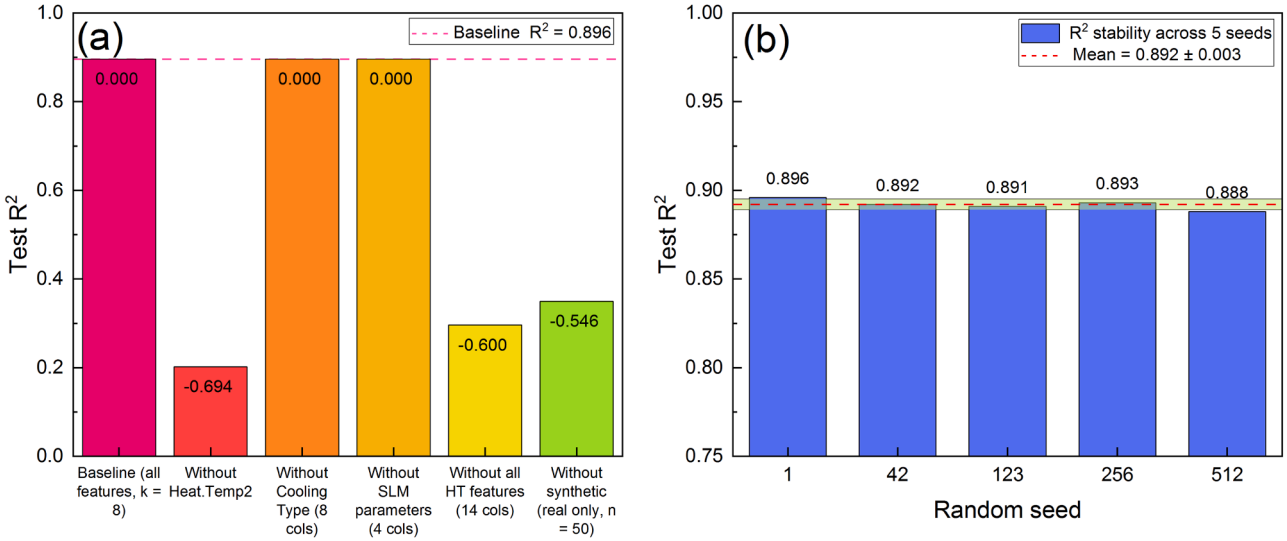

Fig. 7. (a) Feature ablation for VoR model and (b) stability of feature importance for VoR model.

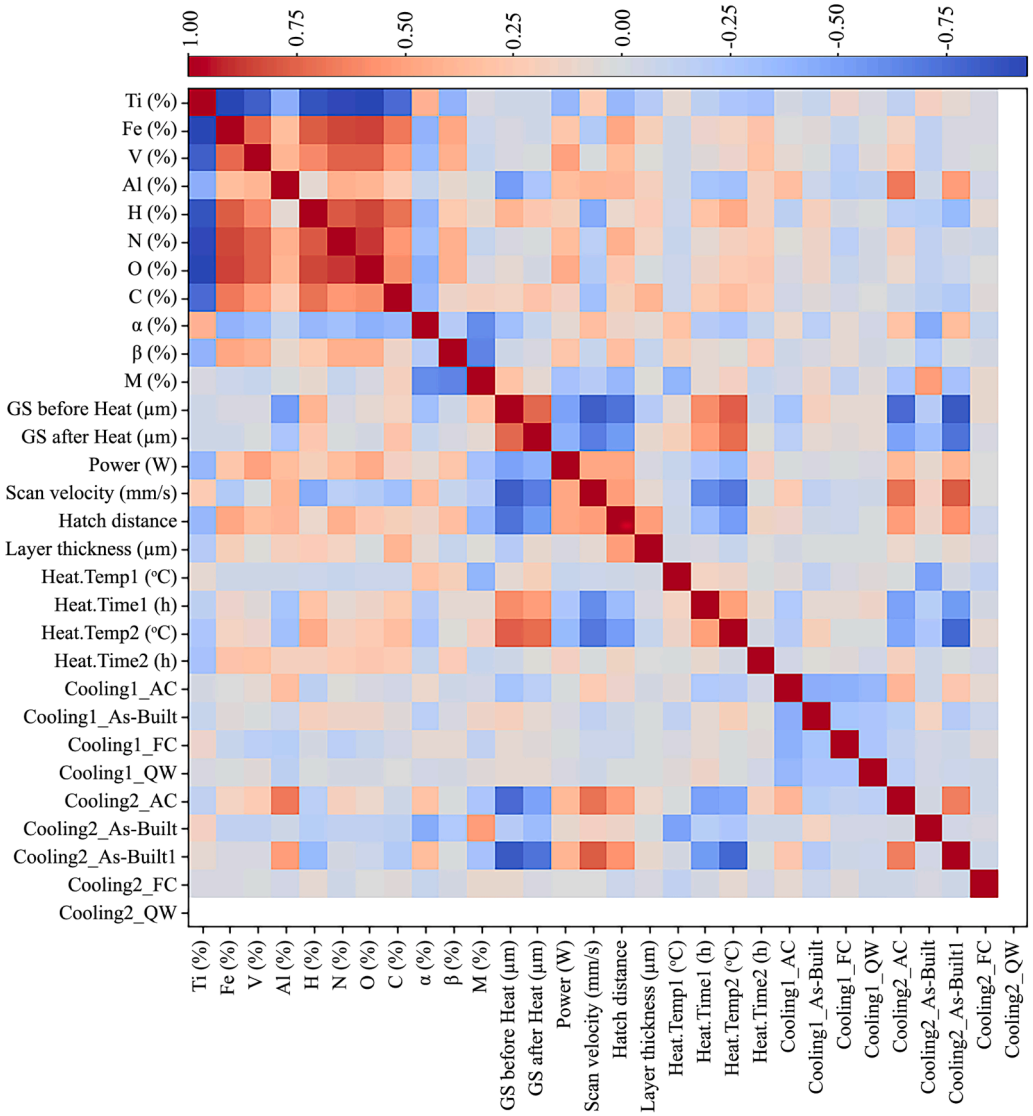

Fig. 8. Pearson correlation heatmap of input features with hardness.

1. Cross-validation, which enabled more reliable evaluation of model performance across different partitions of the dataset.
2. Regularization in the MLP model, which controlled excessive model complexity.
3. Constraints on tree-based models (*e.g.*, maximum depth and minimum samples per split in DT and RF), which prevented uncontrolled growth of trees and the learning of unnecessary details.

The combination of these approaches ensured that the final model not only achieved high accuracy but also demonstrated strong stability and generalization capability.

2.5.6. Implementation

All the models were developed in Python using Visual Studio Code. Key libraries included Scikit-learn for model implementation and evaluation, Pandas for data manipulation, NumPy for numerical computation, Matplotlib for visualization, and XGBoost for GBR models.

3. Results and discussion

3.1. Experimental results

Fig. 9 presents the optical micrographs of the as-built sample. The dominant morphology consisted of alternating bright and dark bands with sharp boundaries, characteristic of an acicular martensitic α′ structure. Along the longitudinal direction (LD), columnar and elongated grains aligned in the build direction were observed, whereas in the transverse direction (TD), the structure appeared flower-like and equiaxed due to the cross-sectional cut perpendicular to the deposited layers. The repetitive, needle-shaped α′ pattern with well-defined spacing reflected the extremely high cooling rate inherent to the SLM process. No evidence of the equilibrium α or β phase was visible, and the colony boundaries were clearly distinguishable. The scattered dark spots were mostly associated with the pores originating from the SLM process. The rapid solidification rate of SLM ($\sim 10^6$ K/s) indeed resulted in non-equilibrium solidification and the formation of acicular α′ martensite [43]. Owing to insufficient time for recrystallization or elemental diffusion, α′ plates formed in an ordered, parallel fashion along the thermal gradient. The absence of the bright β phase regions or stable α colonies confirmed the completeness of the martensitic transformation. Consequently, the as-built alloy exhibited high hardness, whose microstructure could be further modified into a more stable α + β microstructure through subsequent heat treatment. These observations are in close agreement with the observations of Wu *et al.* [44], Khorasani *et al.* [45], and Vrancken *et al.* [46], who also reported the absence of the β phase, lack of stable α regions, and the presence of highly ordered α′

Table 4
Hyperparameters of the VoR model, HGR model, MLP model, and DT model.

Model	Hyperparameter	Values
VoR model	loss	['squared_error', 'absolute_error', 'huber']
	n_estimators	[50, 100, 200]
	max_depth	[5, 6, 7, 8, 10]
	min_samples_split	[2, 4, 6, 8, 10]
	min_samples_leaf	[5, 10, 20]
	subsample	[0.7, 0.8, 0.9, 1.0]
	best_parameters	{'vor__gbr__min_samples_leaf': 8, 'vor__gbr__n_estimators': 250, 'vor__hgbr__l2_regularization': 1.0, 'vor__hgbr__min_samples_leaf': 20, 'vor__weights': [2, 3, 1]}
HGR model	loss	['squared_error', 'absolute_error']
	max_depth	[4,6,8,10]
	learning_rate	[0.05, 0.1, 0.2]
	min_samples_leaf	[10, 20, 30]
	learning_rate	[0.05, 0.1]
	best_parameters	{'hgbr__l2_regularization': 0.0, 'hgbr__learning_rate': 0.05, 'hgbr__loss': 'squared_error', 'hgbr__max_depth': 6, 'hgbr__min_samples_leaf': 10, 'hgbr__n_iter_no_change': 15}
MLP model	hidden_layer_sizes	[(100,), (100, 50), (64, 64, 64)]
	activation	['relu', 'tanh']
	solver	['adam', 'sgd']
	max_iter	[900,1000]
	learning_rate	['constant', 'invscaling', 'adaptive']
	learning_rate_init	[0.001, 0.005, 0.01]
	best_parameters	{'activation': 'relu', 'alpha': 0.001, 'early_stopping': True, 'hidden_layer_sizes': (100, 50), 'learning_rate': 'adaptive', 'max_iter': 1000, 'solver': 'adam'}
DT model	criterion	['absolute_error', 'squared_error', 'friedman_mse']
	max_depth	[3, 4, 5, 6, 7]
	min_samples_split	[5, 10, 15, 20]
	min_samples_leaf	[4, 6, 8, 10]
	best_parameters	{'criterion': 'squared_error', 'max_depth': 4, 'min_samples_leaf': 1, 'min_samples_split': 6}

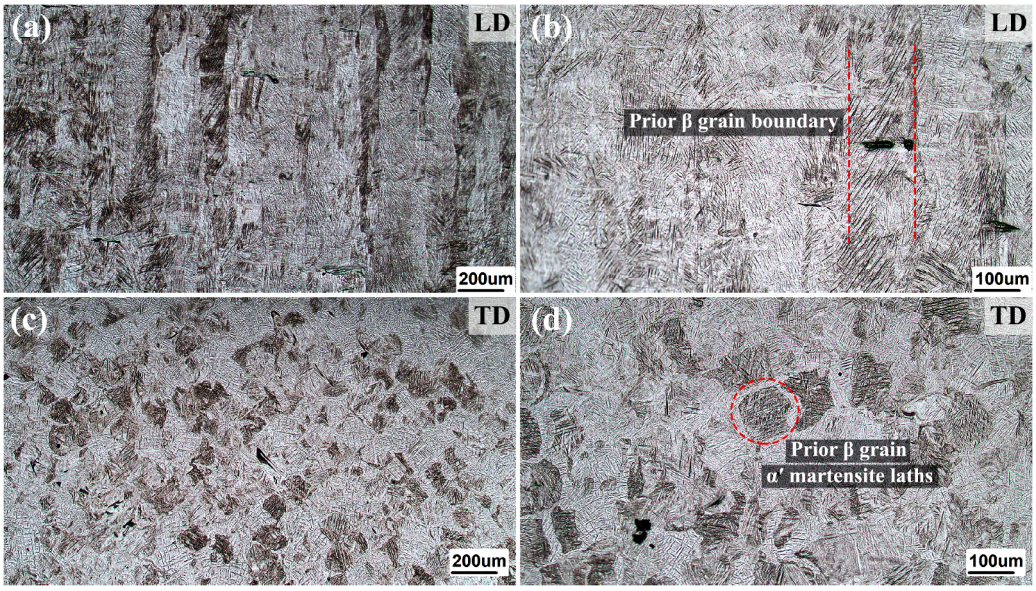

Fig. 9. Optical micrographs of the as-built sample: (a and b) LD and (c and d) TD.

martensite in the as-built SLM-fabricated Ti-6Al-4V alloy.

Figs. 10a, b and c present the optical micrographs of the Ti-6Al-4V alloy heat-treated at 850 °C for 2 h, followed by furnace cooling, in both LD and TD. A highly homogeneous and fully developed lamellar α + β microstructure was observed. Compared with the air-cooled condition (Fig. 10d, e and f), the lamellae appeared to be thicker and more uniform. The α lamellae were well formed and larger than those obtained under other cooling conditions, while the secondary β phase was more extensively developed due to the prolonged diffusion time available during slow furnace cooling. The β phase was evenly distributed as interlamellar precipitates between α lamellae. The directional solidification features, characteristic of the as-built condition, were completely eliminated, and the microstructure was fully recrystallized and homogenized. The heat treatment at 850 °C, followed by FC, therefore, produced the most stable and homogeneous microstructure among the investigated conditions. The α lamellae became coarser, and the β phase was more pronounced and better distributed owing to the extended time for atomic diffusion. Such a condition is considered optimal for applications where ductility and structural stability are prioritized over maximum hardness [25,46,47].

As summarized in Table 5, comparison with the as-built state shows that the heat treatments markedly reduced or even totally removed the needle-like, brittle α′ martensite and replaced it with the stable α and β phases. Increasing the annealing temperature from 750 to 850 °C promoted extensive β formation, thickened the α lamellae and reduced hardness, clearly demonstrating the beneficial role of the heat treatments in rearranging and stabilizing the microstructure of the SLM Ti-6Al-4V.

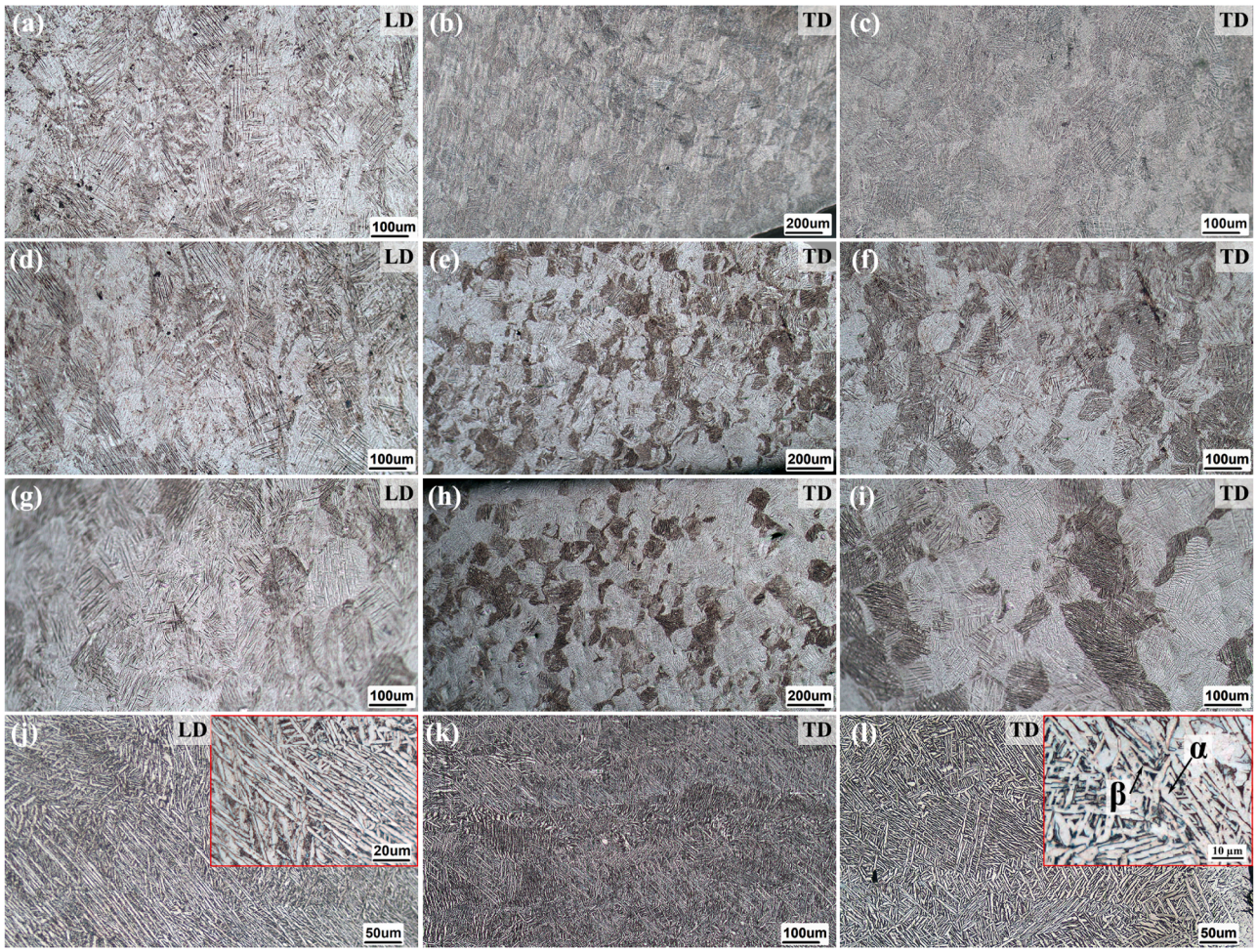

Fig. 10. OM micrographs of the samples after the isothermal and two-stage (duplex) heat treatments, (a-c) 850 °C for 2 h/FC, (d-f) 850 °C for 2 h/AC, (g-i) 850 °C for 2 h/QW, and (j-l) 950 °C for 2 h/QW + 650 °C for 8 h/AC.

Table 5
Microstructural characteristics of the SLM Ti-6Al-4V alloy after different heat-treatment cycles, including phase volume fraction, phase size distribution, and corresponding hardness value.

Sample	Variables	Phase fraction (%)			Lamellae α (μm)	Hardness (HV)
	Cooling condition/time	α′	Secondary β	α lamellar		
As-Built	-	100 %	0 %	0 %	0 %	380±54.63
750 °C	FC	10–20 %	20–30 %	50–60 %	3.5–4	379±32
	AC	30–50 %	10–30 %	15–20 %	2–3	367±20.64
	QW	60 % (Remaining and secondary)	~10 %	~30 %	~1–2 (Extremely narrow)	350±13.1
850 °C	FC	0 %	35–45 %	~55–65 %	2.5–3	386±37.86
	AC	0 %	30–40 %	60–70 %	1–1.5	413.15±17.25
	QW	50–60 % (Rearranged)	5–15 %	~30–40 %	1–1.5	381±7.98
950–650 °C	2 h	0 %	35 %	~65 %	3.5–4.5	354±14.93
	4 h	0 %	40 %	60 %	4.5–5.5	333±4.18
	8 h	0 %	45 %	55 %	5.5–6.5	385±37.91
1050–950 °C	FC	0 %	~40–45 %	~55–60 %	6–7	511.24±99.34
	AC	0 %	~40 %	~60 %	5–6	440±29.51
	QW	0 %	~35 %	~65 %	3.5–4.5	459.1±75

Figs. 10d, e and f show the optical micrographs of the Ti-6Al-4V alloy heat-treated at 850 °C for 2 h followed by AC, on both the longitudinal and transverse sections. A well-developed lamellar α + β microstructure was observed. Compared to the 750 °C condition (AC, not shown in Fig. 10), the lamellae were noticeably thicker, indicating further progression of phase transformation at the higher temperature. The sharp acicular features evident in the lower-temperature and QW samples were almost entirely eliminated, giving way to a fully lamellar morphology composed of the α lamellae with the interlamellar β phase. Enhanced microstructural homogeneity was evident in both of the TD and LD directions, resulting in a more uniform and balanced microstructure. AC suppressed the re-formation of martensite while allowing small regions of the β phase to precipitate between the α lamellae [25].

As a result, a fully lamellar α + β microstructure was formed, free of α′ martensite. In comparison with the heat treatments at a lower temperature (750 °C), the microstructure formed at 850 °C was more

homogeneous and stable. Such well-defined α lamellae with a significant fraction of interlamellar β offer an improved balance between strength and ductility [46–48]. To account for the trend summarized in Table 5, increasing the annealing temperature from 750 to 850 °C (under AC) promoted continuous transformation from the metastable martensitic α′ structure toward a fully stable α + β lamellar morphology, leading to improved phase stability and homogeneity [25,46,47].

Figs. 10g, h and i display the optical micrographs of the Ti-6Al-4V alloy heat-treated at 850 °C for 2 h, followed by QW, observed in both LD and TD. Partial reappearance of acicular α′ martensite was evident. The microstructure consisted of fine, densely packed acicular needles, particularly visible in the darker regions, reflecting the suppressed growth of α + β lamellae during rapid cooling. The α lamellae remained narrow and compressed, indicating insufficient time for their development. Likewise, the β phase did not have adequate time to precipitate or grow, resulting in a microstructure with lower homogeneity, when compared with the furnace-cooled condition. Both TD and LD micrographs revealed a more directional morphology, with less recrystallization and rearrangement. Despite 2 h holding at 850 °C, the rapid cooling rate of QW reintroduced acicular α′ martensite, suppressing the formation and coarsening of the equilibrium α and β phases. Compared with the air- and furnace-cooled specimens, the resulting microstructure was less stable and more brittle, closely resembling the as-built condition but with finer martensitic features. These observations are consistent with the findings of other researchers [25,46–48].

According to Table 5, in the as-built state, the microstructure consisted entirely of α′ martensite, exhibiting high hardness. The heat treatments at 750 and 850 °C, followed by QW, led to re-formation of α′ due to the high cooling rate, although the higher temperature allowed the growth of α and β to a limited extent and the lower temperature led to partial decomposition α′. Compared with 750 °C, the 850 °C condition produced a somewhat more homogeneous microstructure but still it was dominated by fine α′. Overall, decreasing the cooling rate from QW to FC resulted in thicker α lamellae (by approximately 55 %) and better developed interlamellar β. By contrast, QW yielded a finer microstructure likely making the material harder and more brittle, while FC produced coarser, more ductile lamellae.

The microstructure formed at 850 °C, followed by QW, clearly exhibited a mixture of lamellar α + β colonies and residual α′ martensite. This agrees with the findings of Liu *et al.* [49], who reported complete decomposition of α′ into α and β at 850 °C and re-formation of α′ under rapid cooling after annealing. Similarly, Vrancken *et al.* [46] noted that such a condition yielded a morphology closely resembling the as-built microstructure, but with higher density and stronger alignment of α′ needles, leading to increased hardness and reduced ductility.

Fig. 10j, k and l show the optical micrographs of the Ti-6Al-4V alloy subjected to the two-stage (duplex) heat treatment consisting of annealing at 950 °C for 2 h, followed by aging at 650 °C for 8 h and subsequent AC, in both LD and TD. A highly developed and stable lamellar α + β microstructure was evident. Compared with shorter aging durations (*i.e.*, the second-stage) (2 and 4 h), the α lamellae appeared to be significantly coarser, reaching ~5.5–6.5 μm in thickness. The secondary β phase was more extensively developed, appearing wider and more distinct along the lamellar boundaries. The microstructure was homogeneous and free of α′ martensite, with relatively large grains (80–100 μm) and a fully stabilized morphology. The α/β phase ratio appeared nearly balanced, though with a tendency toward increased β fraction relative to shorter aging times. Prolonged aging at 650 °C promoted the coarsening of α lamellae and excessive growth of the β phase, which reduced the hardness but enhanced the ductility and structural stability [44].

As summarized in Table 5, microstructural analysis indicated that increasing the aging time at 650 °C continuously drove lamellar growth and β-phase enrichment, leading to a more homogeneous and stable structure. These changes were accompanied by grain coarsening and reduced hardness. Such trends are in close agreement with the observation made in the previous study [44] that prolonged sub-transus aging enhanced ductility and microstructural stability at the expense of strength.

3.2. Hardness

Fig. 11a illustrates the variation of the hardness values of Ti-6Al-4V with heat treatment temperature under different cooling conditions. The as-built sample exhibited high hardness (~380 HV), attributed to the acicular α′ martensitic structure produced by the extremely high cooling rate during SLM. After annealing at 750 °C, a slight reduction in hardness was observed (~375 HV), while the furnace- and air-cooled samples after annealing at 950 °C showed more pronounced softening (~345 HV). After annealing at 1050 °C, the furnace-cooled sample exhibited the lowest hardness (~315 HV), whereas the AC sample maintained moderately higher hardness values (~330 HV). In contrast, QW resulted in hardness values of ~348–388 HV, reflecting the partial re-formation of α′ martensite. Overall, hardness decreased with increasing annealing temperature, except the samples cooled under the quenching condition, which effectively suppressed excessive softening. This highlights the sensitivity of hardness to cooling rate.

In the experimental procedure, hardness was measured on the sections cut in two different directions, and the measurements were repeated three times in order to minimize errors. However, for the sake of comparability with other studies and to reduce the effect of noise, the average hardness values from the two sections were used as one input for the ML models. Accordingly, the models were trained to predict a single mean hardness value rather than the hardness in each of the directions separately.

Fig. 11b presents the variation of the hardness values of the Ti-6Al-4V samples fabricated by means of SLM and subjected to a duplex heat-treatment. It involved first-stage heating to 1050 °C for 2 h, followed by furnace cooling, and then second-stage heating at 950 °C, followed by cooling at three different rates: FC, AC, and QW, corresponding to samples No. 16, 17 and 18 in Table 2, respectively. Among these samples, the AC sample exhibited the highest hardness (~520 HV), while the FC sample showed the lowest value (~445 HV). The QW sample presented an intermediate hardness (~460 HV) but with a relatively large scatter. These differences can be attributed to the different cooling rates influencing the transformation kinetics of the β-phase. AC and QW cooling leads to the re-formation of martensitic α′, which enhances hardness due to the presence of the fine acicular α' phase with higher dislocation density [50,51], with AC producing an even finer type of the martensite α' phase, as observed by Ldkoadi *et al.* [25]. On the contrary, slow cooling (FC) allows diffusion-controlled decomposition of β into coarser α + β lamellae, reducing hardness because of decreased dislocation density and coarsened α colonies [52]. The slight increase in hardness for QW compared to FC can be related to the re-formation of the metastable phase. Excessively rapid cooling may introduce residual stresses, leading to hardness variability [48].

Overall, the results presented above indicate that appropriate heat-treatment design can enhance the hardness of SLM Ti-6Al-4V beyond the value of the as-built state. Specifically, AC from high temperature (1050 °C), followed by aging (2 h at 950 °C, corresponding to sample No. 17) is the most effective heat treatment scheme for achieving superior hardness (Fig. 11b). This finding aligns with earlier ones concerning the strong sensitivity of SLM Ti-6Al-4V to subsequent heat treatments, which can transform a brittle martensitic structure into a refined α + β microstructure with optimized hardness and strength [53,54].

Fig. 11c shows the results obtained from another duplex heat treatment, in which samples were reheated at 950 °C for 2 h and cooled in furnace, air, or water, followed by an aging treatment at 650 °C for 2, 4, and 8 h (corresponding to samples No. 13, 14 and 15). After aging, all the samples were cooled in air. A time-dependent evolution of hardness was evident: the hardness first increased slightly up to 2 h (~355 HV), decreased at 4 h (~332 HV), and then sharply increased at 8 h (~385

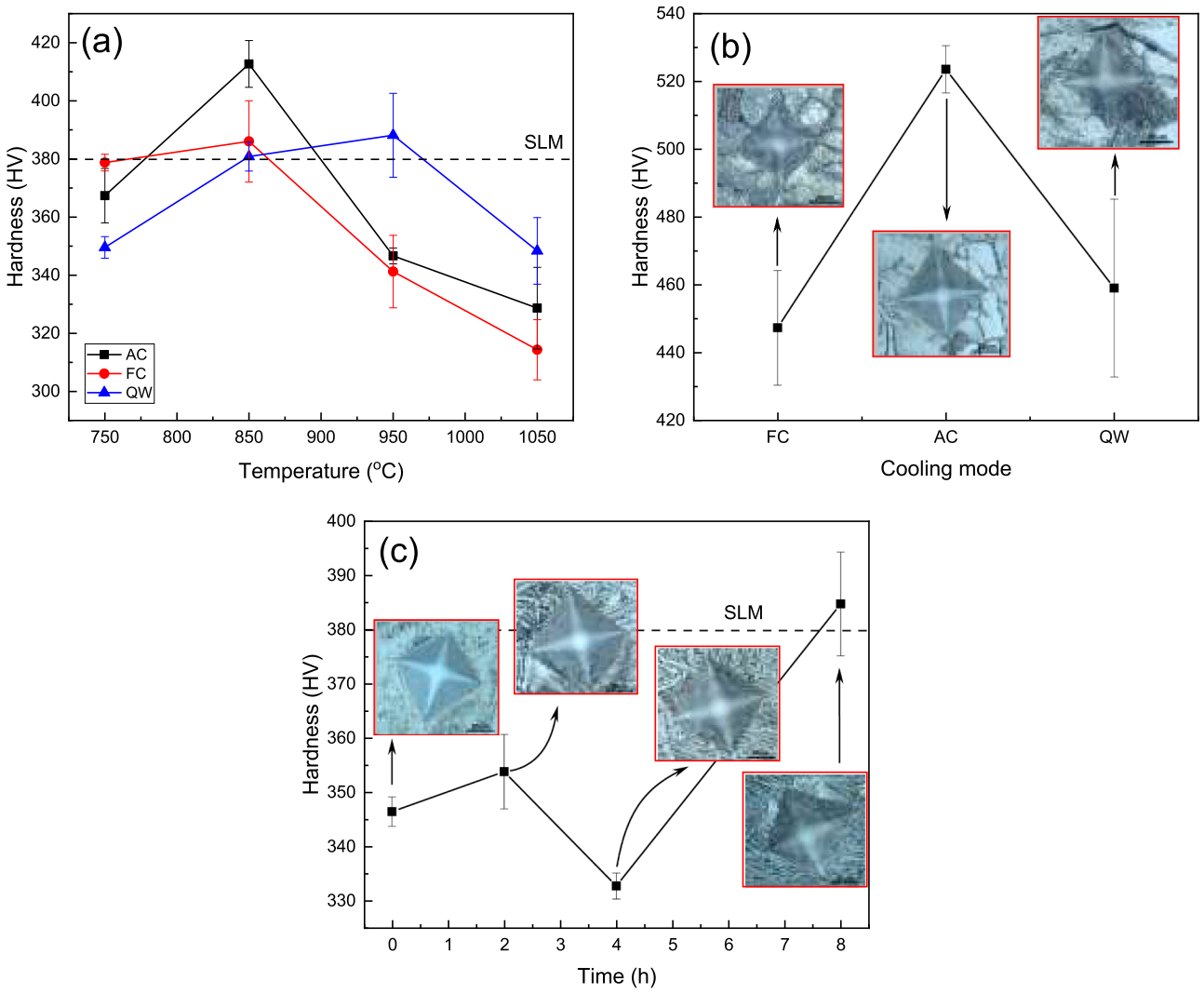

Fig. 11. Hardness variations with the isothermal and duplex heat treatment conditions applied to the SLM Ti-6Al-4V alloy, (a) temperature variable, (b) cooling mode, and (c) time.

HV), exceeding the initial SLM reference hardness (~380 HV). This trend can be explained by the precipitation-strengthening mechanism [55,56]. Within the short timeframe of 2 h, fine secondary α precipitates nucleate within the retained β matrix, resulting in moderate hardening [57]. Prolonged aging (4 h) allows the precipitates to coarsen, reducing hardness. However, after 8 h, more uniform and dense precipitation of the fine α phase within β grains occurs, resulting in significant strengthening and surpassing the hardness of the alloy in the as-SLM state [58,59]. Such precipitation hardening phenomena during the aging of Ti-6Al-4V are well documented, where the balance between the nucleation of fine α precipitates and their coarsening dictates the mechanical response [60]. In short, the observed hardness minimum at ~4 h corresponds to over-aging, while the hardness rise at 8 h indicates a later-stage microstructural evolution (secondary nucleation or transformation) that increases the effective strengthening particle population and/or refines the morphology of these fine precipitates.

The hardness data presented in Table 5 indicate that the microstructure and mechanical response of SLM Ti-6Al-4V are governed by a sequence of dissolution, cooling-rate controlled transformation, and time-dependent precipitation. Solutionizing at ~850 °C produces the finest α + β microstructure and the highest hardness after cooling, whereas higher solutionizing temperatures (≥950–1050 °C) make the final state strongly dependent on cooling route: FC yields coarse α lamellae and the lowest hardness, AC produces a finer α + β structure and the highest, most consistent hardness, and QW gives variable, sometimes high hardness accompanied by large scatter due to retained martensite, heterogeneity and residual stresses [48,50]. The non-monotonic aging response at 650 °C (hardness ↑ at 2 h → ↓ at 4 h → ↑ markedly at 8 h) can be interpreted in light of the distinct starting microstructures created by the different cooling paths after the 950 °C treatment. Furnace cooling produces the relatively coarse equilibrium α phase (with a low dislocation density), air cooling leads to a transformed α + β structure with a moderate dislocation density and retained stresses, and water quenching generates a supersaturated martensitic α′ phase with a very high dislocation density. Accordingly, in sample No. 14 (AC), the decrease in hardness at 4 h could be attributed mainly to precipitate coarsening combined with partial reduction of a moderate dislocation substructure inherited from the solutionizing + AC step. In contrast, sample No. 15 (WQ) retained a high density of defects, enabling a strong precipitation strengthening effect after 8 h, which raised the hardness above the as-built reference.

3.3. *Temperature-dependent phase constitutes*

At 750 °C, partial decomposition of α′ martensite initiates, but remnants remain, especially in water-quenched samples, while a small amount of the β phase appears interlamellarly [44,61]. At 850 °C, nearly complete transformation into α + β lamellae is achieved, with α plates

and interlamellar β clearly observable, and α′ almost eliminated [44,46,61]. At 950 °C, the structure becomes fully stabilized, with coarser α lamellae and expanded β phase, representing a fully equilibrium α + β morphology [44,61]. At 1050 °C, above the β-transus temperature (around 980 °C), coarse β grains form, and upon cooling, α precipitates along β grain boundaries, producing a Widmanstätten structure with thick α lamellae and extensive β. This condition corresponds to the lowest hardness due to excessive coarsening [44,61].

3.4. Temperature-dependent strengthening mechanisms

The observed hardness trends can be explained by the evolution of strengthening mechanisms. In the as-built state, high hardness is primarily derived from the dense α′ martensitic structure and a high dislocation density, thus with dislocation strengthening playing a dominant role. With increasing heat-treatment temperature, progressive decomposition of α′ and formation of α + β lamellae reduce dislocation density, thereby lowering hardness. At intermediate temperatures, phase strengthening (*via* lamellar α + β) and grain refinement contribute significantly to the mechanical response of the alloy. However, at higher temperatures (950–1050 °C), grain coarsening leads to a reduction in the Hall–Petch strengthening effect [62–64], combined with stabilization of the β phase, resulting in a marked hardness decrease.

Overall, the observed microstructural changes and hardness evolution with holding temperature show an excellent agreement with the findings of Wu *et al.* [44] and Xu *et al.* [61], confirming the reproducibility of the phase transformation trends reported in the literature.

3.5. Results from ML models

Different ML algorithms were employed to predict the hardness of the SLM Ti-6Al-4V subjected to various schemes of heat treatment. The models were trained on a combined dataset consisting of experimental measurements, literature-derived values, and synthetically generated data, using a fixed 80/20 train–test split. Key evaluation metrics, including R^2, MAE, and MSE, were calculated to assess prediction accuracy and model generalization. The results demonstrated that ML models could effectively capture the complex, nonlinear relationships between process parameters (*e.g.*, temperature, holding time and cooling rate), microstructural features and the final hardness. These findings highlight the potential of the data-driven approaches to selecting optimal heat-treatment schemes and provide a framework for extending predictive models to other alloy systems.

3.5.1. Baseline model and correlation analysis

To provide a reference for comparison, a simple Dummy Regressor was employed, which predicted the mean hardness of the training set for all the samples without any learning process. As expected, this model yielded a negative R^2 value (−0.000024), while the MAE and MSE values were relatively high, indicating that this model lacks the ability to capture the relationships between the process parameters and hardness. Therefore, the dummy results were used solely as a baseline for comparison with the other ML models.

In parallel, Pearson correlation coefficients were calculated to explore statistical relationships among the input features. As illustrated in Fig. 8, certain process parameters of heat treatment, particularly the first-stage temperature (Heat.Temp1) and second-stage temperature (Heat.Temp2), as well as cooling rates, exhibited strong positive correlations with the resulting hardness. In contrast, post-heat-treatment grain size displayed a negative correlation with hardness, being consistent with the Hall–Petch relationship [62,63]. Among the alloying elements, vanadium (V) showed a moderate influence, whereas Ti and Fe had negligible correlations due to their narrow compositional ranges.

From a metallurgical standpoint, these correlations are fully consistent with the phase transformation behavior of Ti-6Al-4V. Rapid cooling (QW) from elevated temperatures applied during post-SLM heat treatment promotes the re-formation of martensitic α′, thereby increasing hardness, whereas slower cooling stabilizes the equilibrium α + β phases, resulting in reduced hardness. The negative effect of grain coarsening further supports the expected role of microstructural refinement in strengthening. Meanwhile, the weak correlations of alloying elements with hardness highlight dataset limitations, rather than their true metallurgical insignificance.

3.5.2. Model performance comparison

The performance of all the candidate models was systematically evaluated using five-fold cross-validation and an 80/20 train–test split. Hyperparameters were optimized to minimize prediction error and prevent overfitting. Table 6 summarizes the comparative metrics, including R^2, MAE, and MSE values, sorted by R^2. Among the tested algorithms, ensemble approaches demonstrated clear superiority. As shown in Fig. 12, the VoR model consistently achieved the highest predictive accuracy, with the best balance between training and testing performance, indicating minimal overfitting. The close alignment of its predictions with the 45° line underscores its capability to capture the nonlinear dependency of the hardness on the process parameters. The HGR model also showed robust performance, being slightly worse than VOR, but still with stable generalization across unseen data.

In contrast, the DT model exhibited limited accuracy and poor generalization ability. Its predictions were often concentrated around discrete values (*e.g.*, 450 HV), producing a step- like pattern and scattered deviations from the ideal line, particularly at the low and high hardness ranges. These deficiencies stem from the inherent simplicity of the single-tree structures that struggle to handle high variability and nonlinear relationships. Overall, the comparative analysis confirms that the ensemble-based models (*i.e.*, HGR and VoR) provide the most reliable predictive power for this dataset, while single models such as DT remain inadequate for capturing the complex interactions between process parameters, microstructure, and hardness.

A review of the literature reveals that the majority of recent studies on predicting the mechanical properties of Ti-6Al-4V and similar alloys have primarily focused on the application of ML models, such as ANN, SVR, and tree-based approaches including RF and XGBoost. Many of these studies have concentrated on a single mechanical property, such as UTS, YS, fracture toughness, or flow stress, and been limited by small datasets (fewer than 300 samples), collected either from prior publications or from restricted experimental campaigns. A common feature across these studies is that the models were typically trained on the data corresponding to a specific processing condition or a narrow set of parameters, thereby restricting their generalization capability. In particular, the studies, relying solely on simulated data or previously reported datasets, frequently reported quite high accuracies ($R^2 > 0.9$). However, such results do not necessarily guarantee generalization to unseen experimental data. In contrast, the present study focused on predicting one single index of mechanical properties - the Vickers hardness of Ti-6Al-4V and incorporated an expanded set of input features, including SLM process parameters (*e.g.,* laser power and scan speed), heat treatment conditions (*e.g.,* temperature, holding time, and cooling method), and microstructural characteristics. The expansion of input features enabled the ensemble models such as VoR and HGR to achieve higher accuracy than simpler approaches. The results demonstrated that HGR, with a R^2 value greater than 0.9 and low MAE/MSE values, not only captured the overall trends but also maintained reliable generalization across the full hardness range. Notably, this performance was achieved using a mixed dataset that combined experimental measurements with literature data, with an 80/20 train–test split and five-fold cross-validation for validation.

The distinguishing aspects of the present study in comparison to most of the prior studies are as follows:

1. Selection of hardness as the target property - a mechanical characteristic that has received little attention in ML studies (most of prior

Table 6
Predictive performance of benchmarked regression models sorted by R^2. Reported values correspond to independent test-set results after 5-fold cross-validated hyperparameter tuning (80/20 train-test split).

No.	Model	CV R^2	Train R^2	Test R^2	Train MAE	Test MAE	Train MSE	Test MSE	Std. error
1	VOR	0.64	0.925	0.887	7.83	12.81	203.11	266.73	15.00
2	HGBR	0.61	0.937	0.817	6.62	14.55	170.51	431.45	19.40
3	GBR	0.66	0.906	0.642	6.08	21.21	255.64	841.01	22.20
4	XGBR	0.75	0.999	0.629	0.11	24.35	0.02	872.71	29.40
5	KNN	0.75	0.999	0.625	0.001	12.38	13.37	224.26	29.50
6	RF	0.69	0.999	0.622	0.06	5.13	98.43	63.81	29.80
7	DAD	0.72	0.997	0.470	1.72	23.1	8.75	1246.33	35.0
8	ADA	0.77	0.967	0.424	6.25	25.90	90.47	135.565	36.8
9	DT	0.51	0.895	0.374	11.21	26.14	285.63	1473.26	38.1
10	StR	0.75	0.748	0.822	14.03	15.69	682.27	417.50	22.6
11	SVR	0.51	0.594	0.078	24.06	35.71	1099.57	2169.99	45.90
12	LBR	0.31	0.519	0.774	25.38	29.2	1302.55	532.20	22.6
13	SGDR	0.38	0.453	0.661	24.83	19.87	1481.28	798.50	26.9
14	MLP	0.58	0.547	0.053	27.09	40.12	1226.84	2228.91	46.6
15	Dummy Regressor	−0.02	0.00	−0.000024	34.46	37.14	2619.94	2985.379	54.64

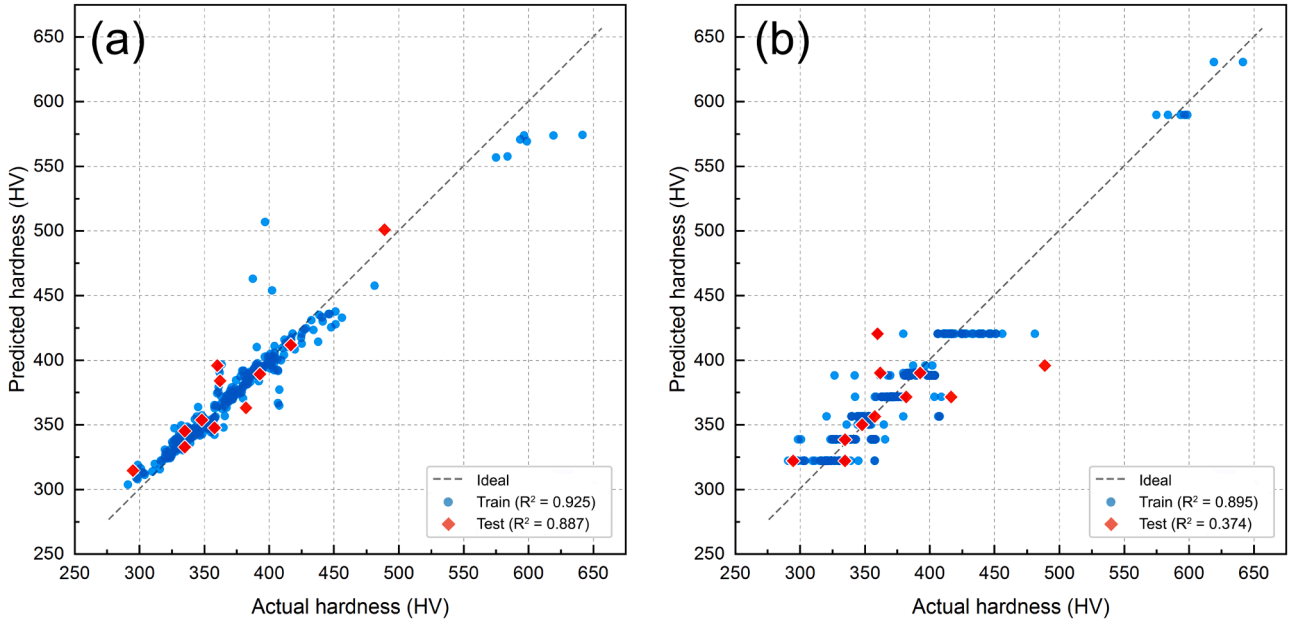

Fig. 12. Actual *versus* predicted hardness values, (a) the VoR model showing a strong agreement with experimental data and (b) the DT model demonstrating limited accuracy and discrete predictions.

studies focusing on strength or flow stress instead). It is actually a unique mechanical property indicating the true effect of microstructural features such as the presence of various phases, precipitate particles, average grain size and alloy composition, unaffected by internal defects inevitably present in SLM parts [65].

2. Integration of both experimental and literature-based data, which enhances the diversity of the dataset and broadens the process and material parameter coverage.
3. Application of ensemble learning methods and feature importance analysis using SHAP values, which not only provides higher predictive accuracy but also offers greater interpretability than the approaches used in other ML studies.

Overall, while most earlier studies concentrate on mechanical properties other than hardness, using classical models and report high accuracy as a result of a narrow scope of the datasets, the present study advances the field by targeting hardness as the output property, leveraging a heterogeneous dataset, and employing ensemble models. This combination delivers improvements not only in prediction accuracy but also in generalization capability and interpretability, positioning this study a step ahead of comparable research.

3.5.3. *Model evaluation protocols*

To ensure statistical rigor and reproducibility, the initial dataset was assembled from two distinct sources, comprising a total of 61 real samples and 30 features. Specifically, 42 samples were collected from published literature covering a wide range of SLM process parameters, and 19 experimental samples were generated in-house under controlled laboratory conditions. The target variable was Vickers hardness (HV). Following initial data preprocessing, which included label harmonization, missing value imputation, and feature encoding, the dataset was partitioned using a stratified 80/20 split. This resulted in a training set of 50 samples and a strictly held-out test set of 11 samples. To prevent any data leakage, the test set was kept completely isolated and was never seen by the models during training, synthetic generation, or hyperparameter tuning.

Recognizing that 50 real training samples were insufficient for robust modeling, data augmentation was applied exclusively to the training set. 200 synthetic samples were generated using Stratified Bootstrap combined with Gaussian Copula Noise. The quality of the synthetic data was

rigorously validated using Kolmogorov-Smirnov (KS) tests and Principal Component Analysis (PCA) to ensure the inter-feature correlation structure and variance of the real data were preserved. Upon successful validation, the extended training set comprised 250 samples. This augmented training data was then normalized using StandardScaler, which was fitted strictly on the training set. During the model development phase, ten different regression models were initially evaluated. To mitigate overfitting, aggressive hyperparameter regularization and feature selection were implemented. Specifically, the SelectKBest algorithm was utilized to reduce the dimensionality from 30 features down to the 8 most informative ones (α %, M %, β %, Heat.Temp1, Heat. Time1, Heat.Temp2, grain size before HT, and grain size after HT).

Hyperparameter tuning for the selected features was conducted using GridSearchCV. Instead of standard K-fold, a ShuffleSplit cross-validation strategy was employed (n_splits = 5, test_size = 0.20) within the extended training set. Ultimately, the final optimized model was subjected to a single, definitive evaluation on the independent test set (11 real samples). The predictive performance of the best-performing model is reported using R^2, Mean Squared Error (MSE), and Root Mean Squared Error (RMSE). The performance metrics reported in Table 6 correspond to the test-set performance unless otherwise specified. To mitigate randomness associated with data splitting, the entire training–testing procedure was repeated with fixed random seeds to ensure reproducibility. Fig. 13

3.5.4. Overfitting assessment and generalization gap

Fig. 14 presents a comparison plot of training and testing R^2 values across the different models. Although certain tree-based models achieved near-perfect fitting on the training set due to their high representational capacity, the generalization gap (Train R^2 − Test R^2) remained within an acceptable range (*e.g.*, <0.05 for VoR). This indicates that the high training performance does not stem from information leakage but reflects the model's ability to capture nonlinear relationships. Furthermore, strict data separation was enforced: preprocessing, synthetic augmentation, and hyperparameter tuning were performed exclusively within the training set to prevent leakage.

3.5.5. Feature importance (SHAP analysis)

The SHAP plot of the VoR, presented in Fig. 15, revealed that the most influential factors in the model's predictions are the parameters used in Microstructure. In particular, the feature M % showed by far the highest importance, with SHAP values indicating that higher values of the microstructure strongly increased the model output. Following this input feature, Heat.Temp2 (°C) and grain size after Heat (μm) were also identified as highly influential features, revealing that longer durations likewise contributed positively to the predictions. These findings highlight that the heat treatment process, especially its temperature and duration, represents the primary driver of the model outcomes.

Other features such as grain size before Heat (μm) and Cooling1_Quench Water also exhibited notable importance, although their effects were considerably weaker, when compared to the heat treatment process parameters and microstructure. In contrast, many other features, including cooling-related parameters (*e.g.*, Cooling1_Furnace Cooling and Cooling1_As-Built) as well as the chemical composition (*i.e.*, the percentages of the elements in the alloy, such as Al, V, Ti, and C), had only negligible influences on the model's predictions. The SHAP values for these features were quite close to zero, indicating that any variations of these parameters would exert virtually no effects on the model output.

The case-specific SHAP waterfall plots provide deeper insights into model behavior. In a well-predicted case (Fig. 15a), the model predicted a hardness value of 395.69 HV, closely matching the experimental value. The most influential factor was M % (+20.53 HV), which directly facilitated α′ martensite formation. Additionally, the grain size after heat treatment contributed positively (+5.46 HV), where the negative normalized feature value indicated a refined grain structure that increased hardness according to the Hall–Petch relationship. In contrast, Heat.Temp2 showed a negative contribution (−5.26 HV), indicating that under certain thermal conditions the second-stage heating temperature may slightly reduce the driving force for secondary hardening. Other factors such as α phase fraction and initial grain size contributed modestly (+4.28 and +1.57 HV, respectively), and their effects were generally consistent with metallurgical expectations.

The top five input features based on the mean absolute SHAP values indicate that microstructural characteristics and heat-treatment parameters play the most significant role in determining the hardness of the SLM Ti-6Al-4V alloy. Among these features, M % stands out as the most influential factor by a considerable margin. Following this feature, grain size after heat treatment and heat-treatment temperatures (Heat. Temp1 and Heat.Temp2) also exert noticeable impacts on hardness values. In addition, certain SLM process parameters, such as hatch distance, exhibit a measurable but comparatively smaller influence. This analysis highlights the strong link between microstructure and mechanical properties, indicating that process parameters primarily affect hardness through their control of phase evolution and grain structure. Therefore, precise design and control of heat-treatment conditions remain key to optimizing the hardness of this alloy, while SLM processing variables play a complementary role. Table 7

In contrast, a poorly predicted case (Fig. 15b) produced a hardness

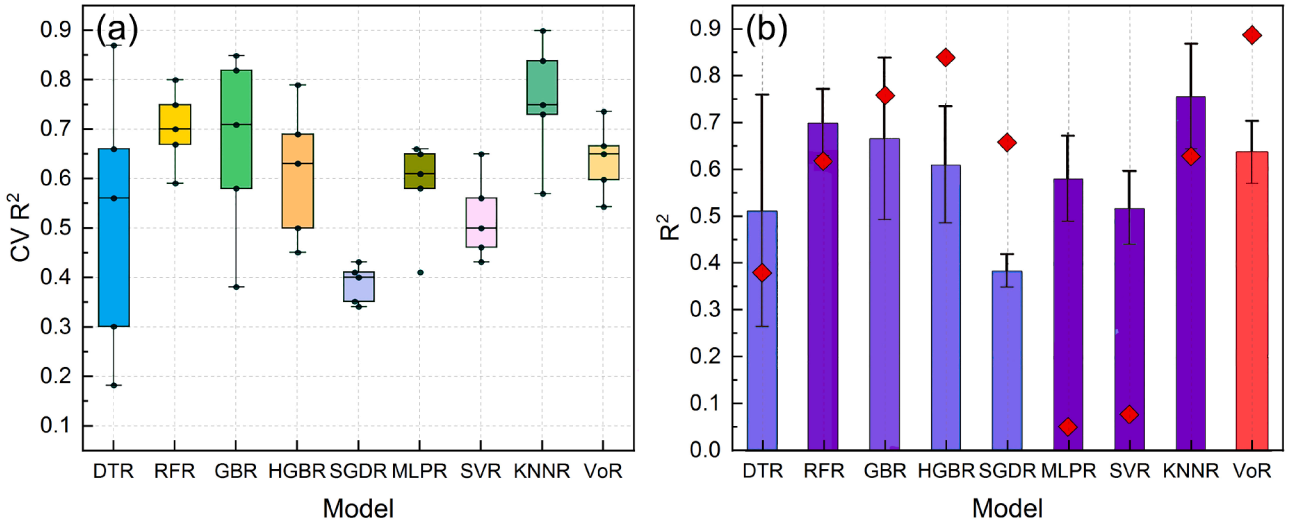

Fig. 13. Cross validation consistency analysis per model: (a) distribution per model, 5-fold Shuffle split and (b) consistency check.

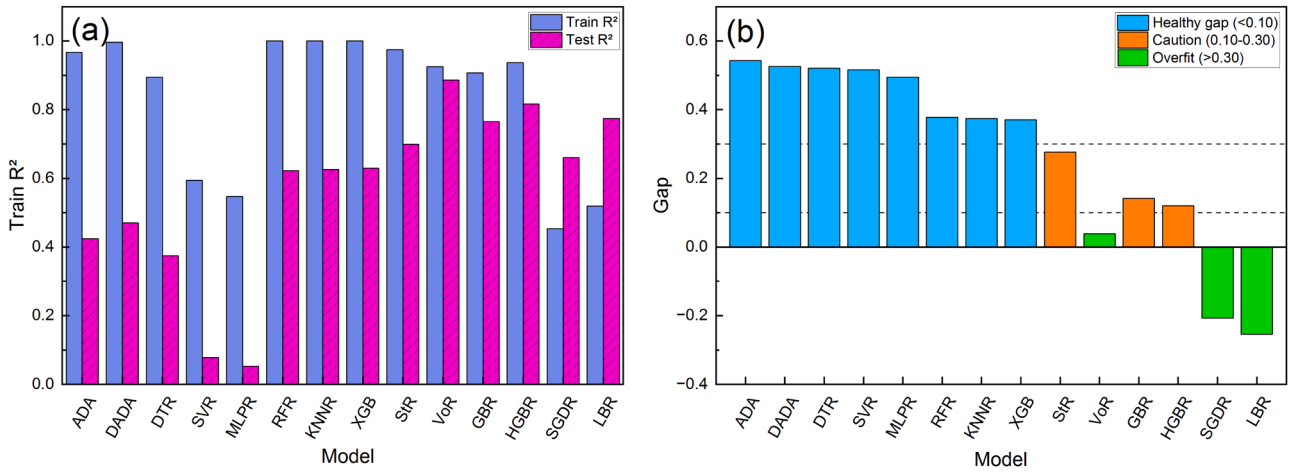

Fig. 14. (a) Comparison plot of training and testing R^2 values across the different models and (b) the generalization gap.

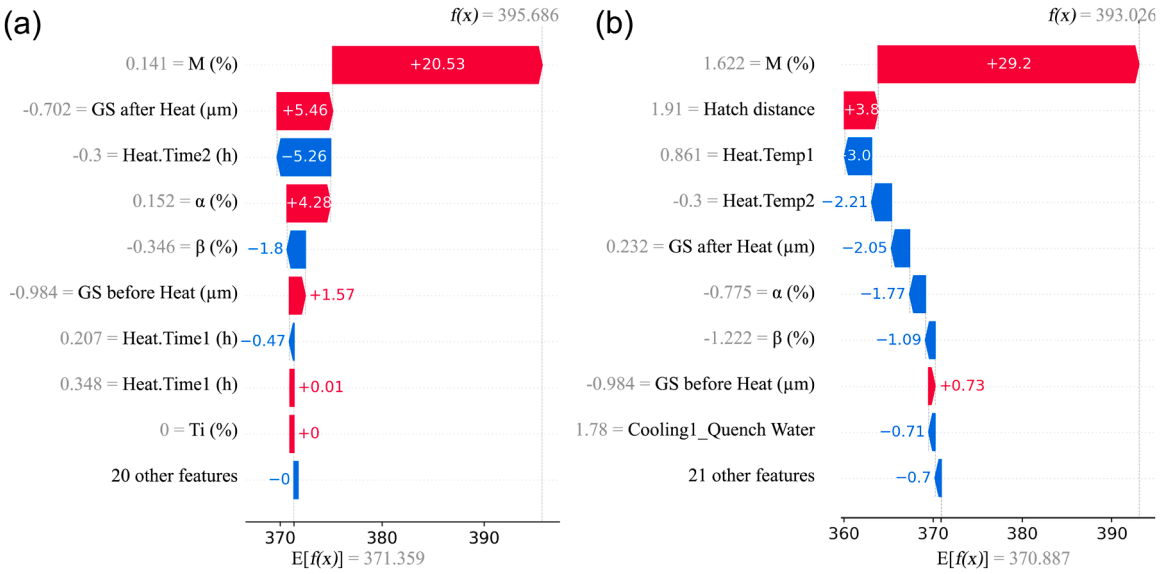

Fig. 15. SHAP analysis of the VoR model, (a) waterfall plot for a well-predicted case and (b) waterfall plot for a poorly predicted case.

Table 7
Top 5 influential features by SHAP.

Rank	Features name	Mean SHAP value
1	M%	20.44
2	Heat.Temp2 (°C)	16.33
3	Grain size after Heat (μm)	3.52
4	Heat.Temp1 (°C)	3.48
5	β%	3.44

prediction of 393.03 HV, which deviated from the experimental measurement. In this case, the strongest positive contribution again originated from M % (+29.2 HV). However, this positive effect was partially counterbalanced by several negative contributions. Elevated Heat.Temp1 and Heat.Temp2 reduced the prediction by −3.0 and −2.21 HV, respectively. Moreover, grain size after heat treatment contributed negatively (−2.05 HV) in this instance, indicating grain coarsening under these specific conditions, which reduced the strength according to the Hall–Petch relationship [62,63]. Interestingly, an SLM parameter, hatch distance, acted as a noticeable positive contributor (+3.8 HV), highlighting that additive manufacturing variables can also influence the predicted properties under certain conditions.

Taken together, the SHAP results confirm that microstructural features, particularly martensite fraction (M %) and grain size, dominate the prediction of hardness, whereas heat-treatment parameters and SLM process variables act as secondary controlling factors. The consistency of SHAP interpretations with established metallurgical mechanisms, including martensitic strengthening and grain-boundary strengthening, supports the reliability of the machine learning model. Furthermore, the varying influence of certain parameters across different cases reflects the intrinsic complexity and non-linear nature of microstructural evolution in SLM-processed Ti-6Al-4V alloys.

In the SHAP beeswarm analysis, the spread of SHAP values for certain features reflects their role in introducing uncertainty in hardness prediction. In particular, the feature Heat.Temp2 exhibited the widest dispersion, ranging from negative to positive values. This indicates that, depending on experimental conditions, this parameter can have either a substantial positive impact or a negative impact on the model output, making it the primary source of uncertainty in the predictions. In contrast, Heat.Time1 and Heat.Time2, although being ranked highly in overall importance, were associated with SHAP values mostly concentrated in the positive range, indicating a more stable and predictable influence on hardness. Similarly, the Grain Size after Heat feature predominantly displayed positive SHAP values, contributing primarily to

the increases in hardness without significant negative dispersion. Therefore, while most process-related features exhibited relatively consistent and unidirectional effects on the predictions, Heat.Temp2 was identified as the main factor contributing to high uncertainty and variability in model performance.

A notable observation from the results is the reduced prediction accuracy under the quenching condition. This can be attributed to several factors. First, quenching in water leads to the formation of a heterogeneous microstructure and high sensitivity of hardness to minor variations in processing conditions, resulting in increased data dispersion and limiting the model's ability to learn stable relationships. Second, the volume of data under the QW condition is smaller, when compared to other process parameters, and this imbalance reduces the model's generalization capability in this domain. Third, the highly nonlinear nature of hardness variation with cooling rate further complicates the identification of precise patterns by the algorithms. Hence, the weaker performance of the models under the quenching condition does not necessarily reflect algorithmic deficiencies but rather the intrinsic complexity of the quenching data.

The SHAP analysis indicates that microstructural features play a significant role in predicting hardness and the ML models are indeed able to effectively capture these relationships. In particular, Grain Size after Heat was identified as a key variable, consistently associated with positive SHAP values. This suggests that grain refinement systematically leads to increased hardness as predicted by the model - a behavior that aligns with established physical and empirical principles, such as the Hall–Petch relationship [62,63]. Moreover, the features related to heat treatment conditions, such as Heat.Time and Heat.Temp, also exert indirect effects on hardness by influencing microstructural evolution. For example, prolonged holding time or higher temperature promotes grain growth and reduces hardness, whereas rapid cooling results in finer microstructures and enhanced hardness. The greater dispersion of SHAP values for some of these parameters, particularly Heat.Temp2, reflects their complex and multifaceted impact on microstructure and, consequently, on hardness, with both positive and negative effects observed, depending on the specific sample.

Overall, these results demonstrate that the ML models not only captured the direct effects of process parameters but also successfully learned their indirect relationships with microstructure and, subsequently, hardness. Therefore, in this study, ML served as a powerful tool that quantitatively modeled the nonlinear, multi-factor interactions between microstructural variables and mechanical properties, providing interpretable and numerical insights into these complex relationships.

3.5.5.1. Comparisons with experimental data and the findings in the literature. The residual plot (Fig. 16a) illustrates the distribution of prediction errors (actual minus predicted values) across the range of predicted Vickers hardness for both the training ($n = 250$) and testing ($n = 11$) datasets. While the vast majority of the data points cluster tightly around the zero-error baseline - indicating highly accurate predictions for hardness values between 300 and 450 HV-a few pronounced negative outliers are visible at higher predicted hardness levels (>450 HV). In these specific instances, the model significantly overestimates the true hardness. These extreme deviations are the primary reason the overall mean residual shifts to approximately −19.23 HV with a standard deviation of about 35 HV, introducing a slight systematic bias toward overestimation.

Fig. 16b complements the scatter plot by displaying the marginal density distribution of these residuals. This density profile clearly demonstrates that the prediction errors for both sets are highly concentrated near zero. The training data distribution exhibits a sharp, narrow peak around the zero line with a long negative tail caused by the few aforementioned outliers. Similarly, the test set residuals display a consistent spread that predominantly falls within an acceptable error margin of roughly ±25 HV. Overall, the visual and statistical evidence suggests that the model effectively captures the underlying relationships between the input features and the output, providing reliable predictions for the bulk of the validation data. However, the localized tendency to overestimate at higher hardness ranges implies that incorporating a larger and more diverse dataset—particularly in those extreme regimes-could help the model generalize better and minimize the remaining prediction errors.

A comparative survey of previous studies, the summary of which is presented in Table 8 and visualized in Fig. 17, reveals that a large variety of ML algorithms have been employed for predicting the mechanical properties of Ti-6Al-4V and similar alloys. Approaches such as MLP, SVR, the k-nearest neighbors (KNN), and random forest regression (RFR) algorithm have frequently been adopted, often relying solely on a limited set of process parameters (*e.g.*, laser power, scan speed, or heat treatment temperature). The reported accuracy values of these models typically range between $R^2 \approx 0.70$ and 0.88. However, due to data limitations and the lack of explicit incorporation of microstructural features, these models often suffer from restricted generalization capability.

In contrast, more recent studies employing ensemble and boosting-based algorithms (such as XGBoost, GBR, or AdaBoost) have achieved higher predictive accuracies (often R^2 >90 %), albeit generally without comprehensive integration of microstructural descriptors. Compared with these studies, the present study demonstrates a notable

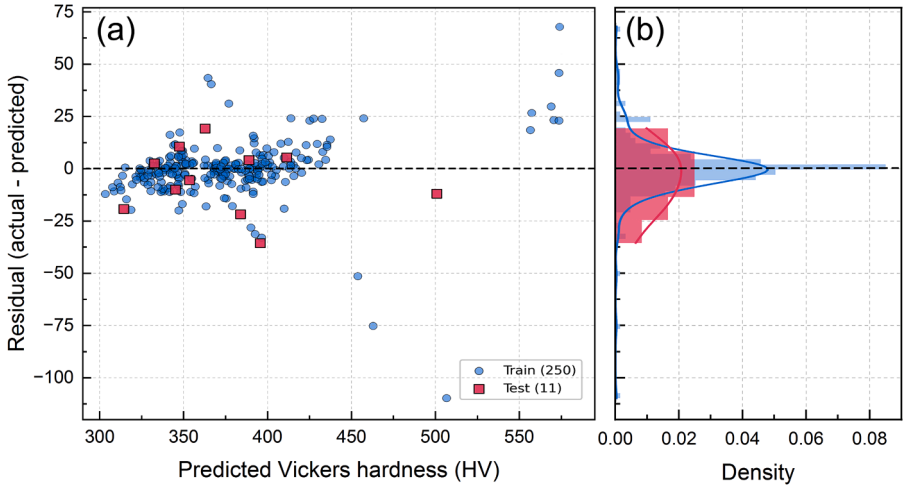

Fig. 16. Residual analysis for the VoR model in Vickers hardness prediction: (a) scatter plot of residuals and (b) marginal density distribution.

Table 8
Summary of the results reported in the literature compared with the present experimental findings.

Model used	Target property	Key inputs	Dataset scale and source	Performance summary	Ref.
Mechanistic ML, PINN + Weibull	VHCF strength & life	SLM process parameters + microstructure + grading strategy	Ultrasonic fatigue tests on SLM Ti-6Al-4V	>50 % design cycle reduction; 20–30 % ↑ crack resistance; strong agreement with Weibull predictions	[70]
MLR, KNN, RF, GPR, ANN, SVM, RBFNN, FL	Tensile strength, tool failure, joint quality	Tool rotation, weld speed, axial force, geometry, plunge depth, torque, current, temp	Large mixed dataset (Al, Ti, steels; exp. + FEM)	ANN $R^2 \approx 0.99$; ANFIS MAPE=7.7 %; performance strongly model-dependent	[71]
ANN (3 models)	UTS, YS, El	Prior-β grain size, α-lath thickness, colony size, vol. fractions	75 literature datasets	YS: $r = 97$ %; UTS: $r = 83$ %; El: $r = 90$ %; high sensitivity to microstructure	[29]
DNN (2-layer FFN)	Grain boundary angle	Crystal growth direction + thermal gradient	4000 simulated + few DED experiments	MSE=0.23 train; ~11° error on experiments	[72]
CIRM (K-means + GPR + SVR + RFR + NSGA-II)	UTS, YS, El	L-PBF parameters + gauge geometry	173 datasets from 31 studies	R^2≈91–92 % for all properties; validated experimentally	[30]
LIN, SVR, RFR, GBR	UTS, YS, El	Bond order, Md, Mo-eq., rolling %, β content	107 β-Ti SMA datasets	El(GBR): train R^2=0.998, test R^2=0.817; UTS unstable across models	[73]
ANN (feed-forward)	UTS, YS, El, microstructure	Composition, HT cycle, t8/5, hardness	Steel alloy dataset (30CrMoNiV5–11)	$R^2 > 90$ % for mechanical & microstructural predictions	[12]
ANN, CNN, GAN, LSTM, GPR, SVM, DT	AM process optimization, defect detection	Nozzle temp, laser power, V, LT, HS	Review of 48 publications (exp. + simulated)	CNN-LSTM accuracy 95 %; CNN 99.38 % in defect detection	[3]
RF, GBR, XGBoost, NN	Grinding forces, T, Ra	Cut depth, table speed, lubrication condition	99 exp. tests on AM-Ti-6Al-4V	R^2 up to 0.99; XGBoost & GBR most stable	[28]
ANN (BP)	Flow stress	Strain, strain rate, T	Hot compression tests (700–1100 °C)	Avg. error ~5.6 %; MAE=5.62 MPa	[27]
GPR (Exp. Kernel), MLR	Relative density	P, V, HS, LT, VED	2900 pub. datapoints + 22 validation samples	GPR MAE=0.27 %; RMSE=0.36 %; MLR significantly less accurate	[11]
RF (best performer)	HEA phase prediction	VED + VEC, ΔHmix, ΔSmix, atomic volume, ΔD	172 HEA datasets + 5 validations	Accuracy 85 %; AUC=0.89–0.95	[74]
KNN, SVM, PCA-KNN, GPR	Fatigue ratio (m), fatigue strength	AM type + process parameters + UTS + HT	FatigueData-AM2022 (Ti-6Al-4V, IN718, AlSi10Mg)	Classification accuracy 91–94 %; RMSE≈0.09	[20]
VOR,HGBR, GBR, XGBoost, AdaBoost, RF, DT, SVR, MLP	Hardness	Chemical composition, microstructure, AM parameters, HT cycle, cooling condition	Experimental (19 samples), literature- (42), and 200 synthetically generated samples via Stratified Bootstrap combined with Gaussian Copula	VOR & HGBR accuracy ≈ 92–93%; stable & low deviation	This work

advancement by simultaneously integrating SLM process parameters, heat treatment conditions, and microstructural descriptors within ensemble models (*i.e.*, AdaBoost and GBR). This strategy yielded predictive accuracies exceeding $R^2 > 0.89$, underscoring the pivotal role of combining microscopic and metallographic information with experimental process data to enhance prediction quality. Furthermore, the application of the hyperparameter optimization techniques (*i.e.*, Grid Search and Cross-validation) effectively mitigated overfitting and improved model stability - an aspect rarely addressed systematically in the literature [66–69].

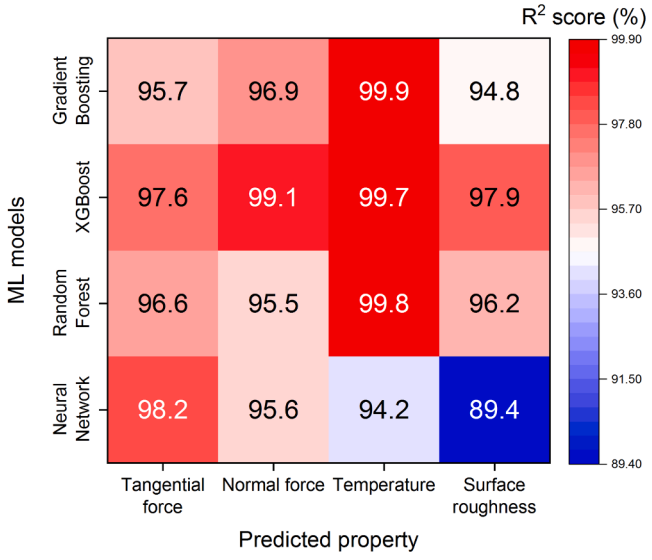

Fig. 17. Heatmap comparison of the reported accuracies of the ML models applied to SLM Ti-6Al-4V. The rows correspond to different ML architectures, while columns represent the predicted outputs [28].

The broader comparative analysis performed in this study also highlights a consistent trend across the field: mechanical property prediction (*e.g.*, UTS, YS, and El %) achieves the highest accuracy (>95 %) when sufficient data is available, whereas microstructural features remain more challenging, with accuracies being close to 85–90 %. This discrepancy is clearly reflected in the heatmap (Fig. 17). Such findings reinforce the need for physics-informed or hybrid frameworks, where governing equations (*e.g.*, heat conduction and phase transformation kinetics) and simulation-derived descriptors (*e.g.*, phase volume fraction, cooling rate, and dislocation density) are embedded into ML pipelines. As discussed earlier, physics-informed machine learning (PIML) approaches, including physics-informed neural network (PINN) and hybrid simulation–ML surrogates, offer promising pathways to reducing overfitting, improving extrapolation to unseen processing/heat-treatment schemes, and enhancing interpretability by aligning model predictions with metallurgical mechanisms.

In summary, while the present work aligns with the trajectory of the prior studies in demonstrating the value of ensemble learners for property prediction, it further advances the field by (i) integrating microstructural descriptors alongside process parameters, (ii) employing robust hyperparameter optimization, and (iii) outlining a clear roadmap toward physics-informed ML. Taken together, these contributions provide both immediate improvements in prediction reliability and a forward-looking framework for developing intelligent, physically grounded models for AM and AM products.

Compared with the prior studies, the present study uniquely integrates heat treatment, including temperature, holding time, and cooling method, into the ML models trained on both experimental and literature-derived data. The prediction accuracy of the VoR model (the highest R^2 and the lowest MAE/MSE among all the tested algorithms) demonstrates that the ensemble-based approaches are particularly effective for capturing the nonlinear influence of thermal processing on hardness. Furthermore, the SHAP analysis provides mechanistic insights consistent with metallurgical knowledge, offering interpretability often missing in earlier purely statistical models.

Despite these advances, several limitations have been identified. First, the dataset included only 19 experimental samples corresponding to 19 distinct processing/heat-treatment conditions with five replicates each. While this design provided statistically valid estimates for the investigated alloy, it constrained the models' robustness and limited their generalizability. Second, the chemical composition was actually constant (Ti-6Al-4V Grade 5), preventing the assessment of the effects of (minor) alloying elements and impurities beyond narrow compositional variations. Third, microstructural descriptors were limited to grain sizes, whereas more advanced techniques such as EBSD or phase volume fraction quantification would be expected to provide richer input features. These constraints underscore the need for expanding datasets with diverse processing conditions and incorporating advanced microstructural parameters in future studies.

In addition, the models were trained solely to predict Vickers hardness, whereas other mechanical properties that are also relevant to engineering and biomedical applications of the SLM Ti-6Al-4V alloy, such as UTS, YS, fatigue performance, and fracture toughness, were not included in the present analysis. Furthermore, no explicit physics-informed constraints (*e.g.*, heat-transfer partial differential equations (PDEs) or phase-transformation kinetics) were embedded in the models. Finally, all the predictions were validated only within the Ti-6Al-4V domain. Direct transferability to other alloys (such as Inconel 718 or Co-Cr alloys) remains untested and will require additional data and model adaptation. These limitations highlight the need for larger, multi-property, multi-alloy datasets and physics-informed ML integration in future studies.

3.6. Future work: PIML

PIML is proposed as a pathway to enhancing robustness and interpretability. While the present study demonstrates the ability of purely data-driven ensemble learners (GBR and AdaBoost) to predict the hardness of the SLM Ti-6Al-4V alloy after heat treatment, the generalization of such models remains limited when the dataset is small or when being extrapolated to unseen heat treatment schemes. A promising direction is to embed governing laws of physics directly into the ML framework. Two approaches are particularly relevant here: (i) PINNs that constrain the training process with heat conduction PDEs and classical phase-transformation kinetics (*e.g.*, Johnson–Mehl–Avrami–Kolmogorov, JMAK), thereby reducing the solution space to physically admissible regimes; and (ii) hybrid simulation–ML surrogates, in which physically based simulations (*e.g.*, based on finite-difference heat transfer models or phase-field calculations) first generate secondary features such as phase volume fractions, lamellar thickness, or dislocation density, which are then fed into data-driven regressors. Such strategies can mitigate overfitting, improve extrapolation to new heat-treatment schemes, and enhance interpretability, since the model's decisions remain consistent with well-established metallurgical mechanisms [75–79].

A schematic representation of the proposed PIML workflow is shown in Fig. 18, where physics-based simulations (heat transfer PDEs, transformation kinetics, and phase-field models) are integrated with experimental, literature-derived, and synthetic data to enrich the feature space before training ML regressors for hardness prediction. This diagram highlights how embedding physics priors can reduce the search space, improve extrapolation, and enhance interpretability of the predictions.

The present models were trained and validated exclusively on the Ti-6Al-4V (Grade 5) data. Direct application of the trained predictors to other alloy systems is not guaranteed, because alloy-specific thermophysical properties, phase constituents and stability, and transformation kinetics strongly mediate the mapping from processing/heat-treatment parameters to resultant hardness. To extend the framework to other alloys, we recommend a combined strategy: (i) augment the dataset with a representative set of the experiments of the target alloy (covering the processing and heat-treatment space), (ii) enrich feature vectors with alloy-specific descriptors (elemental fractions, β-transus or equivalent phase-stability metrics, thermal conductivity (C_p), diffusion activation energies) and physics-derived features (cooling rate, peak temperature, and phase volume fraction) obtained from rapid heat-transfer or phase-field simulations, and (iii) use transfer-learning / domain-adaptation or multi-task models to leverage the knowledge from the Ti-6Al-4V source model while fine-tuning on limited target-alloy data. Such hybrid and transfer-learning strategies have already been shown to improve sample

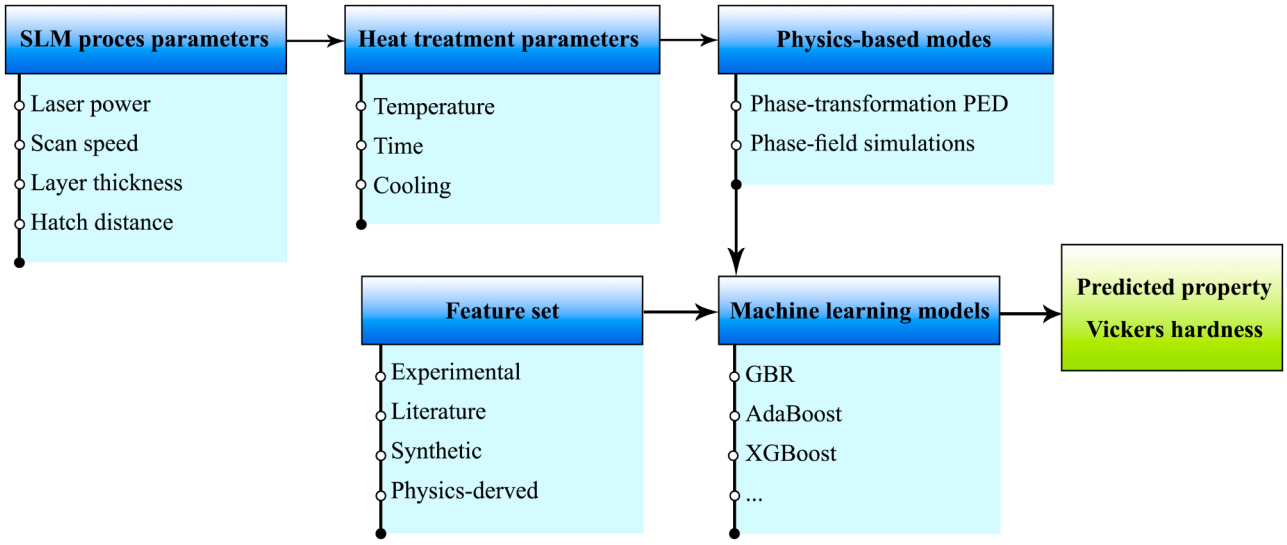

Fig. 18. PIML workflow for the prediction of the hardness of SLM Ti-6Al-4V. Physics-based simulations (heat conduction PDEs, transformation kinetics, and phase-field models) provide additional constraints or features that are combined with experimental, literature, and synthetic data before ML model training.

efficiency and cross-domain performance in addressing materials problems [80–82].

4. Conclusions

This study developed an integrated experimental–computational framework for predicting the post-heat-treatment Vickers hardness of selective laser melted Ti-6Al-4V. By combining curated multi-source data, synthetic augmentation via a Stratified Bootstrap combined with Gaussian Copula Noise, and ensemble machine learning with interpretability analysis, a robust and generalizable predictive model was established. The principal findings are summarized as follows:

The integration of experimental data, literature-derived datasets, and 200 Stratified Bootstrap combined with Gaussian Copula Noise -generated synthetic samples effectively mitigated data scarcity and improved statistical coverage of heat-treatment conditions.

1. Among fifteen benchmarked regression models, the Voting Regressor achieved the highest predictive performance ($R^2 \approx 0.92$; MAE ≈ 7.8 HV), demonstrating strong generalization across diverse thermal treatment parameters.
2. Ensemble learning methods outperformed linear models, confirming the strongly nonlinear coupling between SLM process variables, multi-stage heat-treatment parameters, and resulting hardness.
3. SHAP-based interpretability analysis identified second-stage heat-treatment temperature and holding time as dominant contributors to hardness variation, consistent with α' martensite decomposition, $\alpha + \beta$ phase stabilization, and lamellar coarsening mechanisms reported in the literature.

Collectively, these results demonstrate that data-driven ensemble learning can provide both high predictive accuracy and physically consistent interpretability for post-SLM heat-treatment design. The proposed framework reduces reliance on empirical trial-and-error experimentation and offers a quantitative tool for rational process optimization in industrial additive manufacturing.

Future work should expand the dataset to include broader compositional variations and cooling-rate-sensitive transformations, enabling further improvement in model transferability and predictive robustness.

Prime novelty statement

This work introduces an interpretable, ensemble machine learning framework that integrates experimental, literature-derived, and synthetically generated data to predict the post-heat-treatment hardness of SLM-fabricated Ti-6Al-4V. Unlike prior studies that focus on as-built properties or limited processing variables, the proposed approach explicitly couples SLM parameters, heat-treatment conditions, and microstructural descriptors, while providing physically consistent feature attribution via SHAP analysis. This enables rational, data-driven design of post-SLM heat-treatment schedules with clear engineering relevance.

Funding

No funding was received for conducting this study.

CRediT authorship contribution statement

Alireza Khanlari: Writing – original draft, Methodology, Investigation, Formal analysis, Data curation, Conceptualization. **Ali Reza Eivani:** Writing – review & editing, Project administration, Investigation, Conceptualization. **Morteza Zakeri:** Writing – review & editing, Supervision, Investigation, Formal analysis, Data curation, Conceptualization. **Jie Zhou:** Writing – review & editing, Investigation. **Hamid Reza Jafarian:** Writing – review & editing, Resources, Project administration. **Morteza Tayebi:** Writing – review & editing, Writing – original draft, Supervision, Investigation, Formal analysis, Data curation, Conceptualization.

Declaration of competing interest

The authors declare that they have no known competing financial interests or personal relationships that could have appeared to influence the work reported in this paper.

Data availability

The data that has been used is confidential.

References

[1] L. Zhou, J. Miller, J. Vezza, M. Mayster, M. Raffay, Q. Justice, Z. Al Tamimi, G. Hansotte, L.D. Sunkara, J. Bernat, Additive manufacturing: a comprehensive review, Sensors 24 (2024), https://doi.org/10.3390/s24092668.
[2] T. Pereira, J.V. Kennedy, J. Potgieter, A comparison of traditional manufacturing *vs* additive manufacturing, the best method for the job, Procedia Manuf. 30 (2019) 11–18, https://doi.org/10.1016/j.promfg.2019.02.003.
[3] F. Ciccone, A. Bacciaglia, A. Ceruti, Optimization with artificial intelligence in additive manufacturing: a systematic review, J. Brazilian Soc. Mech. Sci. Eng. 45 (2023) 303, https://doi.org/10.1007/s40430-023-04200-2.
[4] S. Zhao, Y. Shi, C. Huang, X. Li, Y. Lu, Y. Wu, Y. Li, L. Wang, Integrating machine learning into additive manufacturing of metallic biomaterials: a comprehensive review, J. Funct. Biomater. 16 (2025), https://doi.org/10.3390/jfb16030077.
[5] U.M.R. Paturi, S.T. Palakurthy, S. Cheruku, B. Vidhya Darshini, N.S. Reddy, Role of machine learning in additive manufacturing of titanium alloys—A review, Arch. Comput. Methods Eng. 30 (2023) 5053–5069, https://doi.org/10.1007/s11831-023-09969-y.
[6] N. Razavi, B. Van Hooreweder, F. Berto, Effect of build thickness and geometry on quasi-static and fatigue behavior of Ti-6Al-4V produced by electron beam melting, Addit. Manuf. 36 (2020) 101426, https://doi.org/10.1016/j.addma.2020.101426.
[7] J. Dumbre, Z. Tong, Y. Chen, A. Rack, N. Isac, M.V. Upadhyay, M. Easton, D. Qiu, Impact of build process on microstructural evolution in laser directed energy deposition of Ti-8.5Cu alloy: an *in situ* synchrotron X-ray imaging and post-build electron microscopy study, Addit. Manuf. 109 (2025) 104841, https://doi.org/10.1016/j.addma.2025.104841.
[8] K. Wijesinghe, C. Herath, J.G. Michopoulos, S.M. Arnold, A. Achuthan, Hierarchical anisotropic material response of directed energy deposited (DED) Ti-6Al-4V alloy, Acta Mater. 276 (2024) 120080, https://doi.org/10.1016/j.actamat.2024.120080.
[9] E. Stevens, S. Schloder, E. Bono, D. Schmidt, M. Chmielus, Density variation in binder jetting 3D-printed and sintered Ti-6Al-4V, Addit. Manuf. 22 (2018) 746–752, https://doi.org/10.1016/j.addma.2018.06.017.
[10] F.R. Kaschel, S. Keaveney, D.P. Dowling, Comparison between continuous and modulated wave laser emission modes for the selective laser melting of Ti-6Al-4V: dimensional accuracy, microstructure and mechanical behaviour, Addit. Manuf. 55 (2022) 102825, https://doi.org/10.1016/j.addma.2022.102825.
[11] V. Maitra, J. Shi, C. Lu, Robust prediction and validation of as-built density of Ti-6Al-4V parts manufactured via selective laser melting using a machine learning approach, J. Manuf. Process. 78 (2022) 183–201, https://doi.org/10.1016/j.jmapro.2022.04.020.
[12] A. Powar, P. Date, Modeling of microstructure and mechanical properties of heat treated components by using artificial neural network, Mater. Sci. Eng. A. 628 (2015) 89–97, https://doi.org/10.1016/j.msea.2015.01.044.
[13] M. Maleki, A.R. Eivani, M. Tayebi, J. Sherafati, H.R. Jafarian, Correlations in LPBF-fabricated Ti6Al4V: influence of laser power and scanning speed on microstructure and mechanical performance, Results Eng. 29 (2026) 109122, https://doi.org/10.1016/j.rineng.2026.109122.
[14] L. Meng, T. Kitashima, P. Lin, Z. Wang, Z. Jiang, Q. Huang, J. Zhao, Achieving polymer-like ultrahigh elasticity in Ti−6Al−4V alloy via a new cryo-deformation induced α'-to-α'' martensite phase transformation, Acta Mater. 293 (2025) 121109, https://doi.org/10.1016/j.actamat.2025.121109.
[15] J. Hu, Y. Jiang, Y. Yang, H. Xing, F. Han, G. Zhou, K. Zhang, S. Xin, S. Zhang, J. Huang, H. Wang, G. Li, L.-C. Zhang, A. Huang, Formation mechanism of ultrafine $\alpha + \beta$ structure in Ti-6Al-4V alloy during $\beta \rightarrow \alpha m \rightarrow \alpha + \beta$ continuous phase transformation, Scr. Mater. 246 (2024) 116066, https://doi.org/10.1016/j.scriptamat.2024.116066.
[16] S. He, Z. Li, K. Ming, K. Yao, Z. Sun, S. Zheng, Atomic insights into the distinctions between $\{10\bar{1}1\}$ twin boundaries and $[11\bar{2}0]/60^\circ$ boundaries in additively manufactured Ti-6Al-4V, Scr. Mater. 263 (2025) 116679, https://doi.org/10.1016/j.scriptamat.2025.116679.
[17] G. Vashishtha, S. Chauhan, R. Zimroz, N. Yadav, R. Kumar, M.K. Gupta, Current applications of machine learning in additive manufacturing: a review on challenges and future trends, Arch. Comput. Methods Eng. 32 (2025) 2635–2668, https://doi.org/10.1007/s11831-024-10215-2.
[18] V. Blümer, A.R. Safi, C. Soyarslan, B. Klusemann, T. van den Boogaard, Generative 3D reconstruction of Ti-6Al-4V basketweave microstructures by optimization of

differentiable microstructural descriptors, Acta Mater. 291 (2025) 120947, https://doi.org/10.1016/j.actamat.2025.120947.
[19] S. Dhiman, M. Brandt, D. Fabijanic, V. Chinthapenta, W. Xu, Microstructural control across multiple length scales in additively manufactured Ti-6Al-4V via cyclic heat treatments, Acta Mater. 297 (2025) 121372, https://doi.org/10.1016/j.actamat.2025.121372.
[20] S.O. Alfred, M. Amiri, A data-informed knowledge discovery framework to predict fatigue properties of additively manufactured Ti–6Al–4V, IN718 and AlSi10Mg alloys using fatigue databases, Prog. Addit. Manuf. 10 (2025) 6183–6210, https://doi.org/10.1007/s40964-025-00965-1.
[21] S. Gao, X. Yue, H. Wang, Predictability of different machine learning approaches on the fatigue life of additive-manufactured porous titanium structure, Metals (Basel) 14 (2024), https://doi.org/10.3390/met14030320.
[22] J. Li, M. Sage, X. Guan, M. Brochu, Y.F. Zhao, Machine learning-enabled competitive grain growth behavior study in directed energy deposition fabricated Ti6Al4V, JOM 72 (2020) 458–464, https://doi.org/10.1007/s11837-019-03917-7.
[23] A. Yu, Y. Pan, L. Yue, F. Kang, J. Zhang, X. Lu, Explainable machine learning for hardness prediction of laser powder bed fused Ti-6Al-4V and assisting in understanding effects of process parameters, J. Alloys Compd. 1008 (2024) 176566, https://doi.org/10.1016/j.jallcom.2024.176566.
[24] V.M. Kaoushik, U. Nichul, V. Chavan, V. Hiwarkar, Development of microstructure and high hardness of Ti6Al4V alloy fabricated using laser beam powder bed fusion: a novel sub-transus heat treatment approach, J. Alloys Compd. 937 (2023) 168387, https://doi.org/10.1016/j.jallcom.2022.168387.
[25] P. Lekoadi, M. Tlotleng, K. Annan, N. Maledi, B. Masina, Evaluation of heat treatment parameters on microstructure and hardness properties of high-speed selective laser melted Ti6Al4V, Metals 11 (2021), https://doi.org/10.3390/met11020255.
[26] N. Eshawish, S. Malinov, W. Sha, Effect of solution treatment and cooling rate on the microstructure and hardness of Ti-6Al-4V alloy manufactured by selective laser melting before and after hot isostatic pressing treatment, J. Mater. Eng. Perform. 31 (2022) 3550–3558, https://doi.org/10.1007/s11665-021-06489-3.
[27] N.S. Reddy, Y.H. Lee, C.H. Park, C.S. Lee, Prediction of flow stress in Ti–6Al–4V alloy with an equiaxed α + β microstructure by artificial neural networks, Mater. Sci. Eng. A. 492 (2008) 276–282, https://doi.org/10.1016/j.msea.2008.03.030.
[28] A. Anand, S. Kumar, P.K. Singh, Prediction of grinding parameters for additively manufactured Ti-6Al-4V alloy using machine learning techniques, Tribol. Int. 204 (2025) 110512, https://doi.org/10.1016/j.triboint.2025.110512.
[29] A.K. Maurya, P.L. Narayana, J.-T. Yeom, J.-K. Hong, N.G. Subba Reddy, Artificial neural network modeling of Ti-6Al-4V alloys to correlate their microstructure and mechanical properties, Materials 18 (2025), https://doi.org/10.3390/ma18051099.
[30] Y. Cao, C. Chen, S. Xu, R. Zhao, K. Guo, T. Hu, H. Liao, J. Wang, Z. Ren, Machine learning assisted prediction and optimization of mechanical properties for laser powder bed fusion of Ti6Al4V alloy, Addit. Manuf. 91 (2024) 104341, https://doi.org/10.1016/j.addma.2024.104341.
[31] S.L. Lu, Z.J. Zhang, R. Liu, X.H. Zhou, X.G. Wang, B.N. Zhang, X.M. Zhao, J. Eckert, Z.F. Zhang, Optimal tensile properties of laser powder bed fusion hereditary basket-weave microstructure in additive manufactured Ti6Al4V, Addit. Manuf. 59 (2022) 103092, https://doi.org/10.1016/j.addma.2022.103092.
[32] J. Elambasseril, T. Song, S. Mendis, E. Lui, M. Leary, M. Brandt, M. Qian, Effect of powder characteristics on layer density, defects, and tensile properties of Ti-6Al-4V via laser powder bed fusion: establishing benchmark parameters for quality, Prog. Addit. Manuf. 10 (2025) 7449–7470, https://doi.org/10.1007/s40964-025-01046-z.
[33] S. Cacace, A. Capelli, Q. Semeraro, Ti6Al4V Parts fabricated by laser powder bed fusion: tensile behavior and porosity assessment through X-ray computed tomography, procedia CIRP. 138 (2026) 692–697. https://doi.org/10.1016/j.procir.2026.01.119.
[34] J. Radhakrishnan, G. Singh, P. Kumar, N. Nayan, U. Ramamurty, Cryogenic temperature tensile properties of laser powder bed fused Ti-6Al-4V, Materialia 39 (2025) 102307, https://doi.org/10.1016/j.mtla.2024.102307.
[35] S. Dhiman, V. Chinthapenta, M. Brandt, D. Fabijanic, W. Xu, Microstructure control in additively manufactured Ti-6Al-4V during high-power laser powder bed fusion, Addit. Manuf. 96 (2024) 104573, https://doi.org/10.1016/j.addma.2024.104573.
[36] M.Y. Zuo, Y.H. Zeng, K. Sun, J. Sun, M. Wang, Strength prediction and microstructure quantification of Ti-6Al-4V alloy by selective laser melting based on machine learning, Mater. Des. 264 (2026) 115775, https://doi.org/10.1016/j.matdes.2026.115775.
[37] A. Tiwari, in: R. Pandey, S.K. Khatri, N. kumar Singh, P.B.T.-A.I.and M.L.for E. C. Verma (Eds.), Chapter 2 - Supervised learning: From theory to Applications, Academic Press, 2022, pp. 23–32, https://doi.org/10.1016/B978-0-12-824054-0.00026-5.
[38] A. Kocaoğlu, Efficient optimization of a support vector regression model with natural logarithm of the hyperbolic cosine loss function for broader noise distribution, Appl. Sci. 14 (2024) 3641, https://doi.org/10.3390/app14093641.
[39] Y. Altork, Comparative analysis of machine learning models for wind speed forecasting: support vector machines, fine tree, and linear regression approaches, Int. J. Thermofluids. 27 (2025) 101217, https://doi.org/10.1016/j.ijft.2025.101217.
[40] M. Imani, A. Beikmohammadi, H.R. Arabnia, Comprehensive analysis of random forest and XGBoost performance with SMOTE, ADASYN, and GNUS under varying imbalance levels, Technologies 13 (2025) 88, https://doi.org/10.3390/technologies13030088.
[41] K. Zhang, X. Wang, T. Liu, W. Wei, F. Zhang, M. Huang, H. Liu, Enhancing water quality prediction with advanced machine learning techniques: an extreme gradient boosting model based on long short-term memory and autoencoder, J. Hydrol. 644 (2024) 132115, https://doi.org/10.1016/j.jhydrol.2024.132115.
[42] M. Mersha, K. Lam, J. Wood, A.K. AlShami, J. Kalita, Explainable artificial intelligence: a survey of needs, techniques, applications, and future direction, Neurocomputing 599 (2024) 128111, https://doi.org/10.1016/j.neucom.2024.128111.
[43] W.E. Frazier, Metal additive manufacturing: a review, J. Mater. Eng. Perform. 23 (2014) 1917–1928, https://doi.org/10.1007/s11665-014-0958-z.
[44] S.Q. Wu, Y.J. Lu, Y.L. Gan, T.T. Huang, C.Q. Zhao, J.J. Lin, S. Guo, J.X. Lin, Microstructural evolution and microhardness of a selective-laser-melted Ti–6Al–4V alloy after post heat treatments, J. Alloys Compd. 672 (2016) 643–652, https://doi.org/10.1016/j.jallcom.2016.02.183.
[45] A. Khorasani, I. Gibson, M. Goldberg, G. Littlefair, On the role of different annealing heat treatments on mechanical properties and microstructure of selective laser melted and conventional wrought Ti-6Al-4V, Rapid Prototyp. J. 23 (2017) 295–304, https://doi.org/10.1108/RPJ-02-2016-0022.
[46] B. Vrancken, L. Thijs, J.-P. Kruth, J. Van Humbeeck, Heat treatment of Ti6Al4V produced by selective laser melting: microstructure and mechanical properties, J. Alloys Compd. 541 (2012) 177–185, https://doi.org/10.1016/j.jallcom.2012.07.022.
[47] Z.-Y. Zhao, L. Li, P.-K. Bai, Y. Jin, L.-Y. Wu, J. Li, R.-G. Guan, H.-Q. Qu, The heat treatment influence on the microstructure and hardness of TC4 titanium alloy manufactured via selective laser melting, Materials 11 (2018), https://doi.org/10.3390/ma11081318.
[48] L. Thijs, F. Verhaeghe, T. Craeghs, J. Van Humbeeck, J.-P. Kruth, A study of the microstructural evolution during selective laser melting of Ti–6Al–4V, Acta Mater. 58 (2010) 3303–3312, https://doi.org/10.1016/j.actamat.2010.02.004.
[49] J. Liu, J. Liu, Y. Li, R. Zhang, Z. Zeng, Y. Zhu, K. Zhang, A. Huang, Effects of post heat treatments on microstructures and mechanical properties of selective laser melted Ti6Al4V alloy, Metals 11 (2021), https://doi.org/10.3390/met11101593.
[50] T. Vilaro, C. Colin, J.D. Bartout, As-fabricated and heat-treated microstructures of the Ti-6Al-4V alloy processed by selective laser melting, Metall. Mater. Trans. A. 42 (2011) 3190–3199, https://doi.org/10.1007/s11661-011-0731-y.
[51] M. Simonelli, Y.Y. Tse, C. Tuck, Microstructure of Ti-6Al-4V produced by selective laser melting, J. Phys. Conf. Ser. 371 (2012) 12084, https://doi.org/10.1088/1742-6596/371/1/012084.
[52] G. Lütjering, J.C. Williams, Titanium, Springer, 2003. https://books.google.fr/books?id=GwI9ul_wAegC.
[53] B.E. Carroll, T.A. Palmer, A.M. Beese, Anisotropic tensile behavior of Ti–6Al–4V components fabricated with directed energy deposition additive manufacturing, Acta Mater. 87 (2015) 309–320, https://doi.org/10.1016/j.actamat.2014.12.054.
[54] C. Qiu, N.J.E. Adkins, M.M. Attallah, Microstructure and tensile properties of selectively laser-melted and of HIPed laser-melted Ti–6Al–4V, Mater. Sci. Eng. A. 578 (2013) 230–239, https://doi.org/10.1016/j.msea.2013.04.099.
[55] R. Guo, G. Xiong, J. Liu, Y. Wang, D. Davoodi, R. Miri, M. Tayebi, Tribological behavior of Ti-Al-Nb alloy with different Ta additions for high temperature applications, Mater. Lett. 330 (2023) 133324, https://doi.org/10.1016/j.matlet.2022.133324.
[56] C. Xiao, H. Zhang, D. Davoodi, R. Miri, M. Tayebi, Microstructure evolutions of Ti-Al-Nb alloys with different Ta addition, produced by mechanical alloying and spark plasma sintering, Mater. Lett. 323 (2022) 132568, https://doi.org/10.1016/j.matlet.2022.132568.
[57] L. Facchini, E. Magalini, P. Robotti, A. Molinari, S. Höges, K. Wissenbach, Ductility of a Ti-6Al-4V alloy produced by selective laser melting of prealloyed powders, Rapid Prototyp. J. 16 (2010) 450–459, https://doi.org/10.1108/13552541011083371.
[58] X. Zhao, S. Li, M. Zhang, Y. Liu, T.B. Sercombe, S. Wang, Y. Hao, R. Yang, L. E. Murr, Comparison of the microstructures and mechanical properties of Ti–6Al–4V fabricated by selective laser melting and electron beam melting, Mater. Des. 95 (2016) 21–31, https://doi.org/10.1016/j.matdes.2015.12.135.
[59] T. Ahmed, H.J. Rack, Phase transformations during cooling in α + β titanium alloys, Mater. Sci. Eng. A. 243 (1998) 206–211, https://doi.org/10.1016/S0921-5093(97)00802-2.
[60] S.L. Semiatin, T.R. Bieler, The effect of alpha platelet thickness on plastic flow during hot working of TI–6Al–4V with a transformed microstructure, Acta Mater. 49 (2001) 3565–3573, https://doi.org/10.1016/S1359-6454(01)00236-1.
[61] W. Xu, S. Sun, J. Elambasseril, Q. Liu, M. Brandt, M. Qian, Ti-6Al-4V additively manufactured by selective laser melting with superior mechanical properties, JOM 67 (2015) 668–673, https://doi.org/10.1007/s11837-015-1297-8.
[62] Y. Chong, G. Deng, S. Gao, J. Yi, A. Shibata, N. Tsuji, Yielding nature and Hall-Petch relationships in Ti-6Al-4V alloy with fully equiaxed and bimodal microstructures, Scr. Mater. 172 (2019) 77–82, https://doi.org/10.1016/j.scriptamat.2019.07.015.
[63] H. Zhang, F. Liu, G. Ungar, Z. Zheng, Q. Sun, Y. Han, A regime beyond the Hall–Petch and inverse-Hall–Petch regimes in ultrafine-grained solids, Commun. Phys. 5 (2022) 329, https://doi.org/10.1038/s42005-022-01107-7.
[64] M. Tayebi, A.R. Eivani, A. Majididfar, S.A. Parsa, M. Mehdizade, Z. Lalegani, H. R. Jafarian, A review of friction stir welding: from fundamentals to applications with a focus on brass alloys, Mater. Des. (2025) 115358, https://doi.org/10.1016/j.matdes.2025.115358.
[65] J.S. Zuback, T. DebRoy, The hardness of additively manufactured alloys, Mater 11 (2018), https://doi.org/10.3390/ma11112070.
[66] O. Banapour Ghaffari, B. Eftekhari Yekta, M. Zakeri-Nasrabadi, Estimating “depth of layer” (DOL) in ion-exchanged glasses using explainable machine learning, Materialia 33 (2024) 102027, https://doi.org/10.1016/j.mtla.2024.102027.

[67] O. Banapour Ghaffari, B. Eftekhari Yekta, M. Zakeri-Nasrabadi, Designing high-performance ion-exchangeable glasses with multi-objective optimization and machine learning, Ceram. Int. 50 (2024) 42949–42962, https://doi.org/10.1016/j.ceramint.2024.08.141.

[68] A. Ghasemi, A.R. Eivani, O. Banapour Ghaffari, M. Zakeri Nasrabadi, M. Ghosh, S. M. Fatemi, H.R. Jafarian, Machine learning for predicting high-temperature strength of austenitic stainless steels based on composition and deformation parameters, J. Mater. Sci. 60 (2025) 24665–24683, https://doi.org/10.1007/s10853-025-11805-6.

[69] M. Mir, F. Nasirzadeh, M. Zakeri, A. Hill, C. Karmakar, Assessing neural markers of attention during exposure to construction noise using machine learning classification of electroencephalogram data, Build. Environ. 261 (2024) 111754, https://doi.org/10.1016/j.buildenv.2024.111754.

[70] M. Awd, F. Walther, AI-powered very-high-cycle fatigue control: optimizing microstructural design for selective laser melted Ti-6Al-4V, Materials 18 (2025), https://doi.org/10.3390/ma18071472.

[71] A.H. Elsheikh, Applications of machine learning in friction stir welding: prediction of joint properties, real-time control and tool failure diagnosis, Eng. Appl. Artif. Intell. 121 (2023) 105961, https://doi.org/10.1016/j.engappai.2023.105961.

[72] J. Li, M. Sage, X. Zhou, M. Brochu, Y.F. Zhao, Machine learning for competitive grain growth behavior in additive manufacturing Ti6Al4V, MATEC Web Conf. 321 (2020), https://doi.org/10.1051/matecconf/202032103004.

[73] N. Nohira, T. Ichisawa, M. Tahara, I. Kumazawa, H. Hosoda, Machine learning-based prediction of the mechanical properties of β titanium shape memory alloys, J. Mater. Res. Technol. 34 (2025) 2634–2644, https://doi.org/10.1016/j.jmrt.2024.12.244.

[74] D. Chen, J. Guo, L. Guo, X. Tan, Y. Ba, L. Zhang, Q. Zhang, A phase prediction strategy of high entropy alloys manufactured by selective laser melting based on feature selection and machine learning, J. Mater. Res. Technol. 37 (2025) 79–88, https://doi.org/10.1016/j.jmrt.2025.05.122.

[75] M. Raissi, P. Perdikaris, G.E. Karniadakis, Physics-informed neural networks: a deep learning framework for solving forward and inverse problems involving nonlinear partial differential equations, J. Comput. Phys. 378 (2019) 686–707, https://doi.org/10.1016/j.jcp.2018.10.045.

[76] Z. Chen, H. Mu, F. He, L. Yuan, H. Zhu, N. Ma, Z. Pan, A physics-informed machine learning approach for temperature field prediction in metallic additive manufacturing, J. Ind. Inf. Integr. 47 (2025) 100899, https://doi.org/10.1016/j.jii.2025.100899.

[77] M. Faegh, S. Ghungrad, J.P. Oliveira, P. Rao, A. Haghighi, A review on physics-informed machine learning for process-structure-property modeling in additive manufacturing, J. Manuf. Process. 133 (2025) 524–555, https://doi.org/10.1016/j.jmapro.2024.11.066.

[78] K. Shirzad, C. Viney, A critical review on applications of the Avrami equation beyond materials science, J. R. Soc. Interface. 20 (2023) 20230242, https://doi.org/10.1098/rsif.2023.0242.

[79] L. Shang, S. Zheng, J. Wang, J. Wang, Physics-informed neural networks incorporating energy dissipation for the phase-field model of ferroelectric microstructure evolution, ArXiv Prepr. ArXiv2409.02959. (2024).

[80] K. Bartsch, B. Bossen, W. Chaudhary, M. Landry, D. Herzog, Thermal conductivity of Ti-6Al-4V in laser powder bed fusion, Front. Mech. Eng. 8 (2022). https://www.frontiersin.org/articles/10.3389/fmech.2022.830104.

[81] V. Gupta, K. Choudhary, F. Tavazza, C. Campbell, W. Liao, A. Choudhary, A. Agrawal, Cross-property deep transfer learning framework for enhanced predictive analytics on small materials data, Nat. Commun. 12 (2021) 6595, https://doi.org/10.1038/s41467-021-26921-5.

[82] H. Yamada, C. Liu, S. Wu, Y. Koyama, S. Ju, J. Shiomi, J. Morikawa, R. Yoshida, Predicting materials properties with little data using shotgun transfer learning, ACS Cent. Sci. 5 (2019) 1717–1730, https://doi.org/10.1021/acscentsci.9b00804.